Aerodynamic Response of Turbomachinery Blade Rows to Convecting Density Distortions

by

Becky E. Ramer

B.S. Massachusetts Institute of Technology (1994)

Submitted to the Department of Aeronautics and Astronautics
in partial fulfillment of the requirements for the degree of

Master of Science

at the

MASSACHUSETTS INSTITUTE OF TECHNOLOGY

January 1997
[February 1997]

Author .....
Department of Aeronautics and Astronautics
December 20, 1996

Certified by .....
Eugene E. Covert
Professor of Aeronautics and Astronautics
Thesis Supervisor

Certified by .....
Choon S. Tan
Principal Research Engineer
Aeronautics and Astronautics

Accepted by .....
Jaime Peraire
Chair, Graduate Office

Aerodynamic Response of Turbomachinery Blade Rows to Convecting Density Distortions

by

Becky E. Ramer

Submitted to the Department of Aeronautics and Astronautics
on December 20, 1996, in partial fulfillment of the
requirements for the degree of
Master of Science

Abstract

High cycle fatigue is a major failure mode in gas turbine engines. Convecting density distortions have never been considered as a source of unsteady aerodynamic loading on turbomachinery blade rows. A computational investigation of the response of compressor blade rows to convecting density distortions in incompressible flow has been carried out. The goals of this study are to understand the temporal evolution of the density distortions, determine key controlling parametric trends on blade loading, and to investigate the effects of density wake/boundary layer interactions. Inviscid numerical experiments elucidate basic flowfield physics while preliminary viscous numerical experiments show boundary layer interactions.

For the inviscid experiments a planar density wake is introduced into a compressor blade row operating at design point. The density gradients vary from freestream density to some peak value and back to the freestream value. Changes in lift as a wake traverses the passage are characterized by a gradual change in lift starting just before the wake reaches the blade row, reaching a peak value as the density wake passes midchord on the blade, and returning to steady state lift as the wake leaves the blade row. The moment peaks and returns to steady state as the wake traverses the front half of the blade. The moment then goes past steady state and peaks again, returning to steady state as the wake leaves the blade row. Peak loading changes are dependent upon geometry and wake characteristics. The peak in lift coefficient is a function of the steady lift coefficient, a dimensionless density parameter, and the width of the wake compared to chord. The peak in moment characteristic is function of the same dimensionless density parameter, the width of the wake compared to blade chord, the steady moment coefficient, and the blade passage pressure rise. The steady blade loadings and the product of the wake width and dimensionless density parameter follow a linear scaling for density distortions found in the compressor environment.

The density distortion interacts with a boundary layer resulting in a change in the shape of the density distortion and the boundary layer. A low density fluid passing through a blade passage slows at the suction side of the blade where velocities are smaller. The wake travels faster at midpassage and will flow around the bound-

ary layer. This produces circumferential density gradients and thus more vorticity near the boundary layer. Separation occurs sooner because of this vorticity. Downstream of the separation bubble, the lighter fluid produces a thinner boundary layer. This thinner boundary layer near the trailing edge results in greater momentum flux through the passage, but also causes higher heat transfer rates to the blade.

Convecting density gradients have several implications for turbomachinery blade rows. The lift and moment on the blade change as the gradient convects through the passage, scaling for inviscid flows with steady blade loadings, a dimensionless density, and wake width. The gradient also causes thinner boundary layers and early separation on the blade which translates into more unsteady loading effects and changes in performance and heat transfer.

Thesis Supervisor: Eugene E. Covert
Title: Professor of Aeronautics and Astronautics

Acknowledgments

I would like to express my deep gratitude to those whose support, instruction, and guidance have made completing this research possible. First I would like to thank Professor Eugene Covert and Dr. Choon Tan for their patient direction and direction. Their insight and experience were key to making the accomplishment of this projects possible. I would also like to thank Professor Frank Marble for his friendly suggestions and comments. His preliminary work and ideas were the starting point for this research.

The faculty, and staff of the Gas Turbine lab have been a tremendous support in helping my research along and making my stay here a positive experience. Without the computer resources and assistance of Donald Hoyind and Ted Valkov this research would not be possible. I could not have performed these calculations without some support. The majority of the computational work was conducted at the Gas Turbine Laboratorty using computers provided by Professor Epstein. In addition, computer support was obtained from NASA Lewis Research Center. I am extremely appreciative of the computer time and technical support I have received from these resources.

Support for this project was provided by the Air Force Office for Scientific Research(ASOFAR) under contract numer F49620-94-1-0200 and the supervision of Brian Sanders.

I would also like to thank my family and friends who have supported me during this project. First I thank my parents and my brother for their neverending support, encouragement, and faith. I would also like to thank Vince whose love and support have gotten me through many rough patches during this project. The love and support of my best friend Deborah always helped me see the light at the end of the tunnel. One last thank you must go to the guys from the GTL, especially Patia was always available for a chat in the middle of a hectic day.

Contents

List of Figures

Nomenclature

Variables

a	Spatial finite difference coefficient
b	Temporal finite difference coefficient
c	Chord length
	Artificial damping coefficient
h	Local lagrangian interpolant
p	Static pressure
r	Radial direction
s	Coordinate along blade surface
t	Time
u, U	Axial velocity
v	Tangential velocity
w	Width of wake
w_o	Steady state velocity potential due to vorticity
w_1	Velocity potential addition upstream of density change
w_2	Velocity potential addition downstream of density change
x	Axial direction coordinate
y	Tangential direction coordinate
C_m	Factor which has value of 2 when $m = 0, N$ and value of 1 otherwise
E	Integrated error function
M	Mach number
Re	Reynolds number
T_m	Tchebyshev polynomial of order m
α	Angle of attack, angle between flow and axial direction
	Fourier wave number
θ	Circumferential direction
γ	Vorticity distribution on airfoil
λ	Position of density jump

π	Pi
ρ	Density
φ	Velocity potential
ψ	Blade loading parameter
η	Coordinate normal to flat plate
ω	Vorticity
	Complex frequency
μ_o	Coefficient of artificial viscosity
ξ	Coordinate tangential to flat plat
ξ_1	Coordinate of vorticity element
ζ	Complex variable in airfoil plane
$\imath$, $\jmath$	$\sqrt{-1}$
Γ	Circulation
Θ	Wave number
$\Im$	Imaginary
$\Re$	Real

Subscripts

1	Freestream or initial value
2	Perturbation value, inside of density wake
	After density change for Marble's analysis
∞	Freestream value

Operators and Modifiers

$\hat{()}$	Referring to flow update from viscous step
$\hat{\hat{()}}$	Referring to flow update from pressure step
$\tilde{()}$	Fourier Laplace transform variable
$\widetilde{()}$	Nondimensionalized quantity
$()^n$	Referring to flowfield at time step n

Chapter 1

Introduction

This research investigates convecting density gradients as a source of unsteady loading in turbomachinery. These density gradients could come from ingestion of ground surface air, air from hot boundary layers, hot gas sources such as air launched missile exhaust, cold streaks caused by stator blade and freestream temperature differences, and hot streaks from the combustor. As the density gradient convects over a blade, vorticity is generated by the interaction between the density gradient and the blade pressure field. The added vorticity results in time varying forces on the blade. This change in force results in an unsteady lift and moment on the blade, causing fluctuating stresses that contribute to blade fatigue damage.

1.1 Motivation

High cycle fatigue has become a major failure mode in modern gas turbine engines as demand for better performance is placed on designers. The failure mode is caused by an imbalance between the aerodynamic and structural design as the designer strives for increased performance at lower weight. This translates into higher mean stress levels and higher thermal loads on fans, compressors, and turbine blades Thus the designer needs additional information about the properties of materials under these conditions. In particular the designer needs to know if a stress or strain threshold exists after which a flaw in the material will grow to a catastrophic length. The other

side of the problem is the unsteady, aerodynamic loading. Several sources of unsteady aerodynamics have been identified, but unknown sources of loading may still exist.

Several internal and external sources of unsteady aerodynamics exist for turbomachinery. Some external sources which can be ingested in through the inlet include gusts, turbulence, the wake of another aircraft, and the disturbance accompanying a missile launch from an aircraft. The engine is also subjected to unsteady loads from abrupt changes of operating conditions, non-uniform inlet flow caused by the placement of the engine with respect to the airframe, and by unusual angles of flow approaching the fan. Although several external sources contribute to unsteady flow in turbomachinery, many sources of unsteady flow exist inside the gas turbine engine because the internal aerodynamics of the engines is inherently unsteady.

Many sources of unsteady aerodynamics exist inside the gas turbine engine. Fluctuation of blade load can result from rotor-stator interaction, including blade stall and hot streaks from the combustion chamber. Rotor-stator interaction is a source for many unsteady perturbations. As the rotor moves by the trailing edge of the upstream stator, the rotor increases the local angle of attack at the stator trailing edge. As the circulation about the stator responds to this change in angle of attack, the shed vorticity changes and is convected between the stator and rotor. This shed vorticity and the viscous wake from the stator convect to the rotor passage. Because of differences in the temperature of the stator blades and the working fluid, the wake behind the stator has a density variation. Axial vorticity is produced in the passage due to non-uniform blade loading in the radial direction. Thus several sources of unsteady blade loading exist in turbomachinery, but not all of these sources have been studied. The effects of viscous wakes [3, 4] and potential flow interactions [5] on performance have been studied, but convecting wakes and density gradients have not been considered as a source of unsteady excitation in fans and compressors. Although turbine blades are more likely to encounter density gradient, fan and compressor blades are of major concern for this study because they are more susceptible to high cycle fatigue failure.

1.2 Flow Field Physics

Density gradients in the blade row represent a source of loading on the blades when the density gradient is not aligned with the pressure gradient across the blade row. For a density gradient which is lower than freestream density, the loading on the blade decreases. Conversely, a local increase in density causes an increase in blade loading. This can be observed by examining the physics of the flow field.

The unsteady loading caused by density gradients in the blade row is a consequence of equilibrium. Consider a blade row with a convecting density wake (see figure 1.1). In this case the gradient density is lower than the freestream density. A simple analogy to this case is flow in the atmosphere. In the atmosphere low density, higher temperature gases rise to altitudes of lower pressure. Similarly high density, low temperature fluids sink to high pressure areas near the surface of the earth. The same process occurs in the blade row. As the lower density wake moves through the passage, the low density fluid migrates, or flows, toward the suction side of the blade. Thus the wake causes a perturbation velocity impinging on the suction side of the blade. This creates a change in loading on the airfoil. As the density wake convects through the passage the load varies causing vorticity to be shed into the wake. This vorticity will effect downstream blade rows. As the low density fluid flows toward the suction of the blade, the higher density fluid flows toward the pressure side of the blade to satisfy continuity across the density wake. The relative motion of the low and high density fluids produces a pair of counterrotating vorticies in the passage.

The interaction between the density wake and the blade pressure gradient can also be viewed as convecting vorticies. These vorticies influence the elemental vorticies which define the potential flowfield around the airfoil. A linearized potential flow analysis for a convecting density jump encountering an isolated airfoil is presented in section 2.1. Because of the vortex interaction, vorticity on the blade and thus the blade loading change with time. The added vorticity in the passage alters the local velocity gradient on the airfoil. The velocity gradient near the blade surface may increase, causing unsteady heat transfer and separation problems for the blade. To

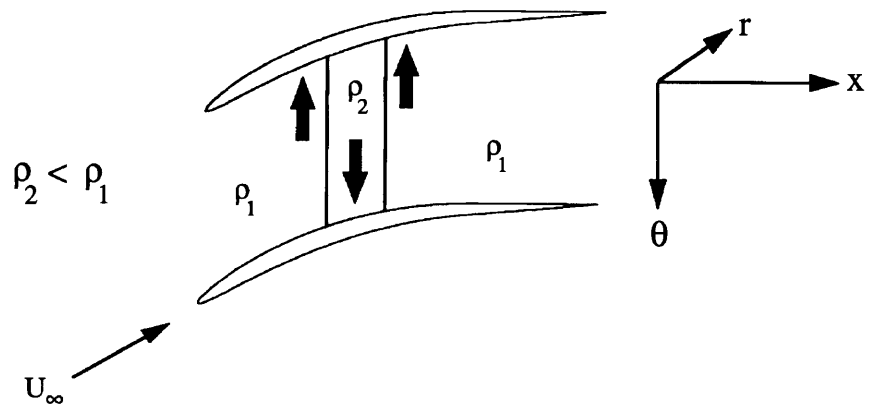

Figure 1.1: Setup of density wake convecting through blade passage.

investigate these problems, computational tools were used to perform a parametric study of the unsteady flow field.

1.3 Technical Approach

This investigation is an exploratory study of convecting density gradients in compressor or fan blade rows. The purpose of the study is to determine the significance of unsteady perturbations caused by the interaction of a convecting density gradient with blade row pressure gradients. The issues to be addressed in this investigation are

1. Investigate the evolution of the density gradient as it convects through the blade passage.

2. Find time varying forces as density distortion convects through passage.

3. Determine dimensionless parameters important to unsteady loading on blade row.

4. Investigate density wake/boundary layer interaction.

Numerical experiments were used to investigate the problem of a blade row in incompressible flow encountering a convecting density gradient. The study was a

two pronged investigation. First inviscid solutions were obtained to gain a basic understanding of the flow physics. The solutions were used to assess the temporal variations in lift and moment caused as the density distortions convect past the blade row. Dimensionless parameters were found which govern these changes in loading. Finally the impact of blade surface boundary layers in the presence of convecting density distortions were examined.

1.3.1 Experimental Parameters

Several calculations were needed to gain an understanding of the problem of density distortion convecting through a blade row. Different test matrices were used for the inviscid and the viscous computational experiments, thus different parameters varied to investigate this problem. For the inviscid test cases two blade geometries were examined, a low loaded NACA blade with most of the pressure change near the leading edge and a higher and more evenly loaded EEE blade. Only the EEE blade was used in the viscous tests. The blade spacing, Reynolds number, and flow angle of attach were held as a constant for inviscid flow, but the Reynolds number was varied for the viscous flow. For the unsteady density wake, similar wake widths and internal density structures were used in both studies.

Two different forms of density gradient were studied for inviscid flow. The first had a sinusoidally varying density, changing from a freestream density ρ_1 to a peak density ρ_2 and back to freestream. The other form of density wake will be referred to as a 'flat top'. The flat top wake has an abrupt sinusoidal change from ρ_1 to ρ_2 then remains at the peak density ρ_2 for some distance, and abruptly returns in the same manner to the freestream density. For viscous flow only the sinusoidal form of the density variation was investigated. A test case for either viscous or inviscid flow is characterized by one wake entering the passage and convecting normal to the blade row.

1.3.2 Contributions

The goals of this study are to understand the temporal evolution of the density distortions, determine key controlling parametric trends on blade loading, and to investigate the effects of density wake/boundary layer interactions. Inviscid numerical experiments elucidate basic flowfield physics while preliminary viscous numerical experiments show boundary layer interactions. Convecting density gradients are found to have several implications for turbomachinery blade rows. The lift and moment on the blade change as the gradient convects through the passage, scaling for inviscid flows with steady blade loadings, a dimensionless density, and wake width. The gradient also causes thinner boundary layers and early separation on the blade which translates into more unsteady loading effects and changes in performance and h at transfer.

1.3.3 Thesis Overview

This introductory chapter reviewed the importance of density gradients as a source of unsteady load, explained the basic physics involved in this problem, and outlined the technical objectives and approach. Chapter two is dedicated to a theoretical understanding of the problem. A linearized theoretical analysis performed by Frank Marble [6] is explained, which is then used to non-dimensionalize the important equations for this problem. Chapter three outlines the computational tools used for this study. The following two chapters outline blade response to the convecting density distortion first through an inviscid blade row, then through a blade row with a blade surface boundary layer. The inviscid blade results show significant changes in lift and moment as the distortion convects through a blade passage. The magnitude of these changes can then be scaled with characteristics of the density wake and steady blade loadings. The viscous results show interaction between the density distortion and the boundary layer which change boundary layer characteristics, and change the position of separation on the blade. Finally chapter six concludes the thesis with important implications of inviscid and viscous of flow results. This chapter also includes rec-

ommendations for future work which will add to the physical understanding of the problem.

Chapter 2

Theoretical Analysis

The main previous work done on the study of density gradients as a source of unsteadiness is by Frank Marble [6]. He performed a linearized potential flow analysis for a flat plate at angle of attack encountering a sharp density jump. This analysis gives a basic understanding of the parameters involved in this problem, thus contributing to a dimensional analysis of the problem.

2.1 Potential Flow Analysis

The idea of density gradients as a source of unsteady loading was initiated by Frank Marble of Caltech [6]. He performed a linearized theoretical analysis for the response of a thin airfoil encountering a strong density discontinuity. Marble used a potential flow analysis to find the response of an isolated flat plate at an angle of attack encountering a sharp density step.

2.1.1 Introduction

If the fluid is treated as incompressible and the velocity disturbances caused by the airfoil are small compared to freestream velocity, the density field can be expressed as $\rho(x - Ut, \eta)$. Vorticity is generated by the interaction of the convected density with the pressure field generated by the airfoil. For a continuous density distribution in

two dimensional flow, this vorticity satisfies the relation

$$\left(\frac{\partial}{\partial t} + U\frac{\partial}{\partial \xi}\right)\omega = \frac{1}{\rho^2}\nabla p \times \nabla \rho \tag{2.1}$$

Therefore if the density gradient($\nabla\rho$) is large(zeroth order), the vorticity is of the same order as the pressure field of the airfoil.

Following Marble's work the response of a plane lifting airfoil to the passage of a strong density discontinuity normal to the direction of motion of the main stream is explained in this chapter. As the density discontinuity encounters the airfoil, a vortex sheet is formed on the discontinuity where it is generated at a rate proportional to the pressure gradient. The problem is formulated through representing the airfoil as a sheet of vortex elements whose distribution must satisfy boundary conditions on the airfoil in the presence of i). the vortex sheet shed from the trailing edge of the airfoil and ii). the vorticity generated in the freestream by non-uniform density. Thus techniques from conventional thin airfoil theory are used with the introduction of some novel features. One of these novel features concerns the linearized field generated by a single vortex element in the presence of a strong plane density jump as the jump convects with a uniform freestream velocity parallel to the horizontal axis. A very convenient representation of this field is presented which simplifies determination of the vorticity distribution on the airfoil. A second novel issue is introduced because Kelvin's theorem may not be applied in the usual fashion for this problem. However, by considering local impulse generation of airfoil loading, the relationship between airfoil circulation and shed vorticity may be represented in a form identical with that for an airfoil in a uniform density field.

2.1.2 Calculation of Potential

For a uniform fluid an element of vorticity $\gamma(\xi_1)d\xi_1$, where $\gamma(\xi_1)$ is the vorticity distribution on the airfoil, has a complex potential

$$w_o(\zeta, t) = \imath\frac{\gamma(\xi_1, t)d\xi_1}{2\pi}\ln(\zeta - \xi_1) \tag{2.2}$$

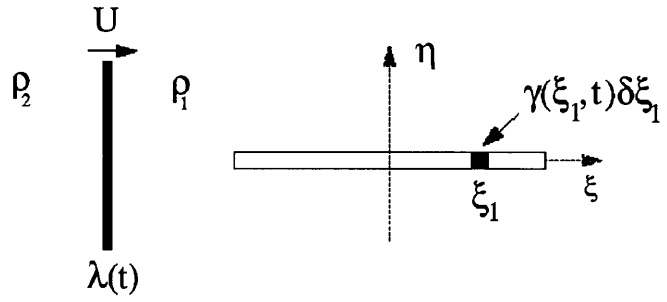

Figure 2.1: Test setup for Marble's theoretical analysis.

where $\zeta = \xi + i\eta$ is the complex variable in the airfoil plane and ξ_1 is the coordinate of the vorticity element. When a density jump from freestream ρ_1 to ρ_2 enters the flow field from the left, see figure 2.1, the potential has a discontinuity at $\xi = \lambda(t)$, but is regular on either side. Therefore the solution requires two additional velocity potentials, one for $\xi > \lambda$ and one for $\xi < \lambda$. The boundary conditions which must be satisfied are the additional potentials must vanish in the far field, produce equal values of the ξ-velocity component at $\xi = \lambda[u(\lambda, t)]$, and produce equal values of pressure on either side of the discontinuity $p_1(\lambda, \eta) = p_2(\lambda, \eta)$. These pressure perturbations satisfy the Bernoulli integral

$$\frac{\partial \varphi_i}{\partial t} + U\left(\frac{\partial \varphi_o}{\partial \xi} + \frac{\partial \varphi_i}{\partial \xi}\right) = \frac{p_i}{\rho_i} \tag{2.3}$$

Satisfying the boundary condition for the pressure at $\xi = \lambda(t)$ gives

$$\rho_1\left(\frac{\partial \varphi_1}{\partial t} + U\frac{\partial \varphi_1}{\partial \xi}\right) - \rho_2\left(\frac{\partial \varphi_2}{\partial t} + U\frac{\partial \varphi_2}{\partial \xi}\right) = (\rho_2 - \rho_1)\left(\frac{\partial \varphi_o}{\partial t} + U\frac{\partial \varphi_o}{\partial \xi}\right) \tag{2.4}$$

A more detailed explanation of the solution for these potentials is given in reference [6]. For this study only the added potential due to vorticity will be examined because only changes in vorticity cause changes in loading. These added potentials have the nature

of partial images of the actual vortex element and are

$$w_1(\zeta,t) = i\frac{\gamma(\xi_1,t)d\xi_1}{2\pi}\left(\frac{\rho_1-\rho_2}{\rho_1+\rho 2}\right)\ln\left((\zeta-\lambda)+(\xi_1-\lambda)\right) \tag{2.5}$$

$$w_2(\zeta,t) = i\frac{\gamma(\xi_1,t)d\xi_1}{2\pi}\left(\frac{\rho_1-\rho_2}{\rho_1+\rho_2}\right)\ln\left((\zeta-\lambda)-(\xi_1-\lambda)\right) \tag{2.6}$$

for $\xi_1 > \lambda$, the case shown in figure 2.1. For $\xi < \lambda$ the complex potential is $w_o + w_1$, and for $\xi > \lambda$ the complex potential is $w_o + w_2$. Both potentials consist of the original vortex plus a coincident vortex of strength $(\frac{\rho_1-\rho_2}{\rho_1+\rho_2})$ times the original strength. When the density jump has moved downstream of the vortex element $\lambda > \xi_1$, the corresponding supplementary potentials are

$$w_1(\zeta,t) = i\frac{\gamma(\xi_1,t)d\xi_1}{2\pi}\left(\frac{\rho_1-\rho_2}{\rho_1+\rho 2}\right)\ln\left((\zeta-\lambda)-(\xi_1-\lambda)\right) \tag{2.7}$$

$$w_2(\zeta,t) = i\frac{\gamma(\xi_1,t)d\xi_1}{2\pi}\left(\frac{\rho_1-\rho_2}{\rho_1+\rho 2}\right)\ln\left((\zeta-\lambda)+(\xi_1-\lambda)\right) \tag{2.8}$$

From these potentials Marble finds that the total vorticity on the density jump is

$$\int_{-\infty}^{\infty}\gamma_\lambda(\eta) = \frac{\gamma(\xi_1,t)}{2\pi}\left(\frac{\rho_1-\rho_2}{\rho_1+\rho_2}\right) \tag{2.9}$$

the strength of the "image vortex" employed to construct the solution.

2.1.3 Unsteady Forces

To compute the forces on the blade, the added vorticity on the blade caused by the density jump must be computed. For steady flow the vorticity distribution $\gamma_o(\xi_1)$ is assumed known. For this problem, additional components of downwash are induced at the airfoil by i) vorticity on the density discontinuity and ii) the wake vorticity resulting from the unsteady character of the convective motion of the density field. The concept of using an image vortex pertains only to vorticies that are in relative motion with respect to the density jump or whose strength varies with time. Wake vorticies, however, are stationary with respect to the density discontinuity and of con-

stant strength. Because of this the image vortex method cannot be used to compute the influence of the extra components of downwash. This additional downwash then necessitates a supplementary vorticity distribution, $\gamma_1(\xi_1)$ on the airfoil to satisfy the boundary conditions.

At each point ξ on the airfoil, the induced vertical velocity at the surface must cause the fluid to move tangentially to the airfoil surface. The steady vorticity distribution on the blade, $\gamma_o(\xi_1)$, already satisfies this condition. Consequentially the remaining induction must give zero vertical velocity on the blade. The remaining induction falls into three categories:

1. Direct induction of supplementary vorticity distribution on blade.

2. Induction of vorticity distribution on density jump resulting from airfoil vorticity $\gamma_o(\xi_1) + \gamma_1(\xi_1, t)$.

3. The induction of wake vorticity.

Using the airfoil boundary conditions, time varying vorticity on the blade can be found. A general, analytic solution for the vorticity was not given by Marble. He instead used computational methods to integrate his analytical equations which were based on satisfying the boundary conditions on the flat plate. This gave solutions for the lift and moment on the flat plate as a density jump convects along the airfoil. In figures 2.2 and 2.3 the lift and moment for a density change of $\frac{\rho_2}{\rho_1} = 0.5$ are plotted. The values for lift and moment excluding the effects of induction are plotted as dotted lines. The features of this problem will be described with reference to the lift coefficients. As the density jump approaches within about one half chord of the leading edge, the induced downwash generates a reduction of airfoil vorticity distribution, and consequently a lift reduction. As the discontinuity passes the leading edge, a strong upwash is produced, creating a situation resembling a sharp-edge gust. The subsequent rise in C_L overshoots the value of C_{Lo} because of poor numerical spatial resolution. The moment coefficient, see figure 2.3, reflects these events in local loading. The response as the density jump passes off the trailing edge is relatively

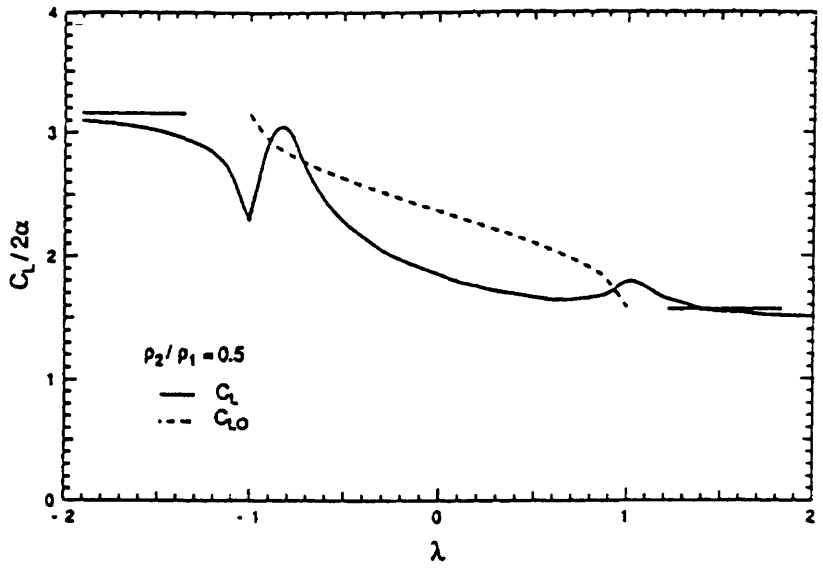

Figure 2.2: Lift coefficient during passage of density discontinuity over the airfoil, $\frac{\rho_2}{\rho_1} = 0.5$.

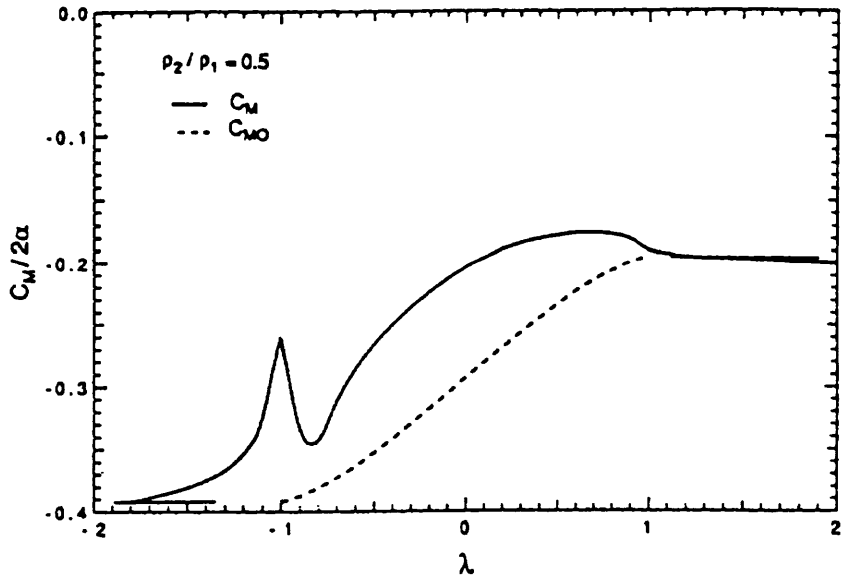

Figure 2.3: Moment coefficient during passage of density discontinuity over the airfoil, $\frac{\rho_2}{\rho_1} = 0.5$.

mild because the value of vorticity is smaller in this region, consequently the near-field reflection is small.

2.2 Dimensional Analysis

Because scaling parameters are important and useful in engineering and scientific evaluations, a dimensional analysis is essential. Several methods for performing a dimensional analysis exist. Three methods for finding dimensionless parameters are by finding similarity solutions for the problem, using the Buckingham π theorem, or through an understanding of the physics of the problem. The physics involved in a density wake moving over a flat plate airfoil was used to non-dimensionalize basic equations.

The momentum equation is non-dimensionalized to find important parameters for this problem. An understanding of the physics of the flowfield outlined in 2.1 is essential to this analysis. In particular, the density parameter $(\frac{\rho_2-\rho_1}{\rho_1+\rho_2})$ from Marble's linearized potential flow analysis should be a key parameter to this flowfield. Another important variable is the width of the strip. Remembering these parameters for the dimensional analysis gives

$$\frac{\partial \widetilde{u}}{\partial \widetilde{t}} + \frac{w}{c}\widetilde{u} \cdot \widetilde{\nabla}\widetilde{u} = -(\frac{\rho_2 - \rho_1}{\rho_2 + \rho_1})\widetilde{\nabla}(\frac{\widetilde{p}}{\widetilde{\rho}}) + \text{viscous terms} \tag{2.10}$$

where the new dimensionless variables are

$$\widetilde{p} = \frac{p}{(\rho_2 - \rho_1)U_\infty^2} \tag{2.11}$$

$$\widetilde{u} = \frac{u}{U_\infty} \tag{2.12}$$

$$\widetilde{t} = \frac{U_\infty}{w}t \tag{2.13}$$

$$\widetilde{\nabla} = \frac{\nabla}{c} \tag{2.14}$$

$$\tilde{\rho} = \frac{\rho}{\rho_1 + \rho_2} \tag{2.15}$$

This gives two important dimensionless parameters, $(\frac{w}{c})$ and $(\frac{\rho_2 - \rho_1}{\rho_1 + \rho_2})$.

These two parameters are key variables in this computational experiment. Another important parameter for this study is Re, the Reynolds number. The Reynolds number determines the boundary layer thickness and how turbulent the flow is. The three important dimensionless parameters for this problem are $(\frac{w}{c})$, $\rho^* = (\frac{\rho_2 - \rho_1}{\rho_1 + \rho_2})$, and Re.

Chapter 3

Computational Tools

Two separate computational tools were used to investigate this problem. Both tools solve the Navier-Stokes equations. An incompressible spectral element solver with pseudo-inviscid boundary conditions yielded inviscid solutions to the perturbation flow. A finite difference solver was then used to investigate the effects due to interaction between the density wake and the blade surface boundary layer. These codes were chosen because they are higher order methods which give time accurate results with high spatial resolution.

3.1 Spectral Solver

A spectral Navier-Stokes solver written by Theodore Valkov [9] was used to obtain incompressible, pseudo-inviscid results. The Navier-Stokes equations are non-dimensionalized to freestream values giving:

$$\widetilde{\nabla} \cdot \tilde{u} = 0 \tag{3.1}$$

$$\frac{\partial \tilde{u}}{\partial \tilde{t}} = -\tilde{u} \cdot \widetilde{\nabla}\tilde{u}\widetilde{\nabla} + \tilde{p} + \widetilde{\nabla}(\frac{1}{Re})\widetilde{\nabla}\tilde{u} \tag{3.2}$$

for laminar flow. The equations are made dimensionless by normalizing all distances by the stator blade chord c_x, normalizing velocities by the axial freestream velocity U_∞, normalizing the pressure by freestream dynamic head $(\rho U)_\infty$, and measuring time

in units of $(\frac{c_x}{U_\infty})$. From this point the tildes no longer be used in this section, even thought he variables are still dimensionless. In the right hand side of equation 3.2, the first term represents the convection of the flow, the second term is the pressure, and the third is the effect of viscosity. These terms are solved for separately in the time stepping scheme.

3.1.1 Time Discretization

This spectral solver uses a fractional time splitting scheme. Starting from an initial flowfield, the scheme updates flow variables at each time increment in three fractional steps. The first step is the convective step which calculates the change in velocity from time t to time $t+\Delta t$ due to convective effects only. The step uses a fourth order Runge-Kutta method to solve:

$$\hat{u}^{n+1} = u^n - \int_t^{t+\Delta t} u \cdot \nabla u dt \tag{3.3}$$

This velocity is next updated with the pressure step

$$\hat{\hat{u}}^{n+1} = \hat{u}^{n+1} - \int_t^{t+\Delta t} \nabla p^{n+1} dt \tag{3.4}$$

using a backward Euler discretization. A pressure field p^{n+1} yields an updated velocity that satisfies continuity. The third and final step, the viscous step, updates the velocity to account for dissipation in the flowfield. An implicit Crank-Nicholson Scheme discretizes

$$u^{n+1} = \hat{\hat{u}}^{n+1} - \int_t^{t+\Delta t} (\nabla (Re) \nabla u) dt \tag{3.5}$$

while applying Dirichelet boundary conditions. This three step scheme has an error of $O(\Delta t)$. It may become unstable if the time step is too large for the given grid resolution and Reynolds number.

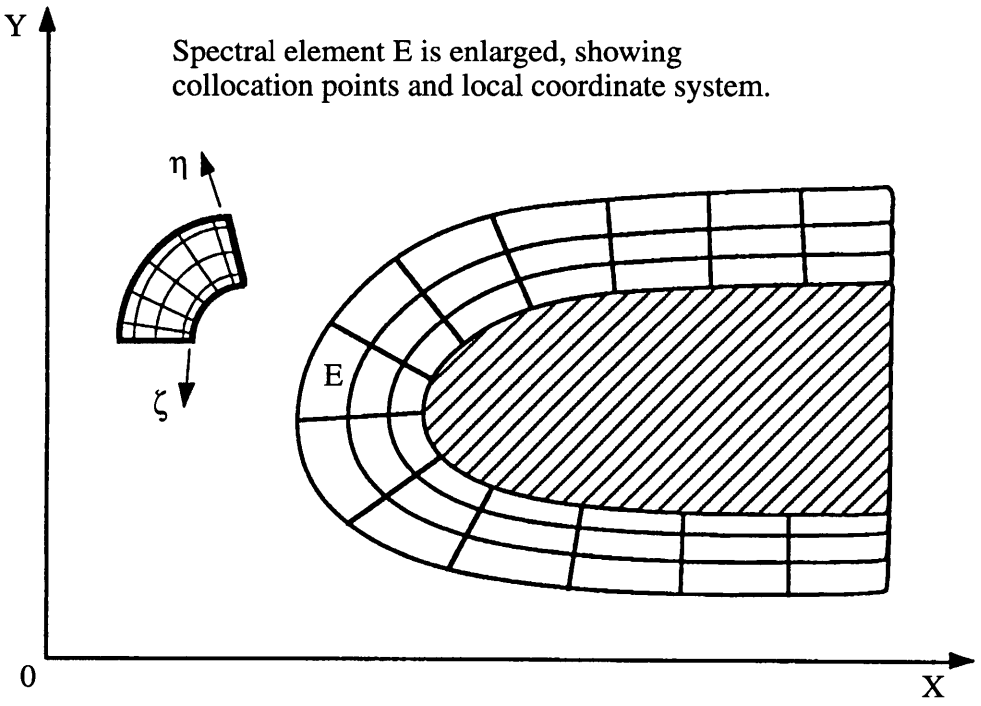

Figure 3.1: Example of Spectral element gridding technique.

3.1.2 Spatial Discretization

The spatial discretization is performed by dividing the computational domain into spectral elements. Inside each spectral element(see figure 3.1),the flow variables are expanded in a series of local Lagrangian interpolants:

$$\left\{ \begin{array}{c} u \\ p \end{array} \right\} = \sum_{j=0}^{N} \sum_{k=0}^{N} \left\{ \begin{array}{c} u_{j,k} \\ p_{j,k} \end{array} \right\} h_j(\zeta) h_k(\eta) \tag{3.6}$$

where $u_{j,k}$ and $p_{j,k}$ are velocity and pressure values at the collocation point $()_{i,j}$ in each element. These local interpolants are based on Chebyshev polynomials:

$$h_n(s) = \frac{2}{N} \sum_{m=0}^{N} \frac{1}{\bar{C}_m \bar{C}_n} T_m(s_n) T_m(s). \tag{3.7}$$

The natural set of coordinates (ζ, η) local to each element is related to the physical coordinate system (x, y) by an isoparametric tensor-product mapping. The coordinates

of the collocation points in the local coordinate system are

$$(\zeta, \eta)_{j,k} = (\cos\frac{\pi j}{N}, \cos\frac{\pi k}{N}) \tag{3.8}$$

During the discretization process, the periodic boundary conditions are implicitly implemented. To accomplish this the computational grid is generated so that nodes on the upper and lower boundaries have the same abscissas. A unique index, $()_{j,k}$, is then used for pairs of matching nodes on the periodic boundaries.

3.1.3 Boundary Conditions

As stated in the previous section, periodic boundary conditions are implemented on the upper and lower boundaries. The inlet boundary condition for the field is prescribed by a velocity profile. The outflow boundary condition is a simple extrapolation which assumes that the flow does not evolve in the streamwise direction aft of the outflow boundary.

$$\frac{\partial u}{\partial x}(x_o, y, t) = 0 \tag{3.9}$$

For the tests performed in this study, the flow is laminar. The spectral solver can compute turbulent flowfields at $Re \geq 10,000$ using a Baldwin-Lomax Turbulence model.

The original code written by Valkov assumed a constant density flow. Philippe Deregal modified the code to allow for incoming density wakes. Because of difficulty in altering incompressible code to allow for density changes, a slip boundary condition was imposed on the blade. This alleviates problems caused by the interaction between the density wake and the boundary layer on the blade because the boundary layer on the blade has been eliminated.

3.2 Finite Difference Solver

A finite difference Navier-Stokes solver written by Donald Hoying [2] was used to study the interaction between the density perturbation and the boundary layer on

the blade. Although the code was written for compressible flows, it was run at a low Mach number ($M = 0.2$) to simulate incompressible flow. Hoying's code was chosen because it uses a dispersion preserving scheme which is a higher order method that yields time accurate results with high spatial resolution.

3.2.1 Discretization

Instead of choosing discretization methods which produce highly accurate results, a method was chosen which has optimal dissipation and dispersion characteristics. This method, described by Tam and Webb [8], is referred to as a Dispersion Relation Preserving (DRP) scheme. The DRP scheme defines spatial and time discretization. Starting with a general description of a first derivative on a uniform grid gives:

$$\left(\frac{\partial f}{\partial x}\right)_i \simeq \frac{1}{\Delta x} \sum_{l=-N}^{M} a_l f(x + \Delta x) \tag{3.10}$$

In traditional finite difference schemes the coefficients a_l eliminate terms from the Taylor's series expansion of f. Instead an approximation to the derivative in equation 3.10 is considered in Fourier transform space. A Fourier transform of equation 3.10 gives

$$\imath\alpha\tilde{f} \simeq \left(\frac{1}{\Delta x} \sum_{l=-N}^{M} a_l e^{\imath\alpha l\Delta x}\right) \tilde{f} \tag{3.11}$$

From this a numerical approximation for $\alpha\Delta x$ is defined as

$$\alpha\Delta x \simeq \bar{\alpha}\Delta x = -\imath \sum_{l=-N}^{M} a_l e^{\imath\alpha l\Delta x} \tag{3.12}$$

where $\bar{\alpha}\Delta x$ represents the finite difference approximation of $\alpha\Delta x$. To obtain the best approximation of the derivative, the error function E should be minimized.

$$E = \int_{-\Theta_o}^{\Theta_o} |\alpha\Delta x - \bar{\alpha}\Delta x|^2 d(\alpha\Delta x) \tag{3.13}$$

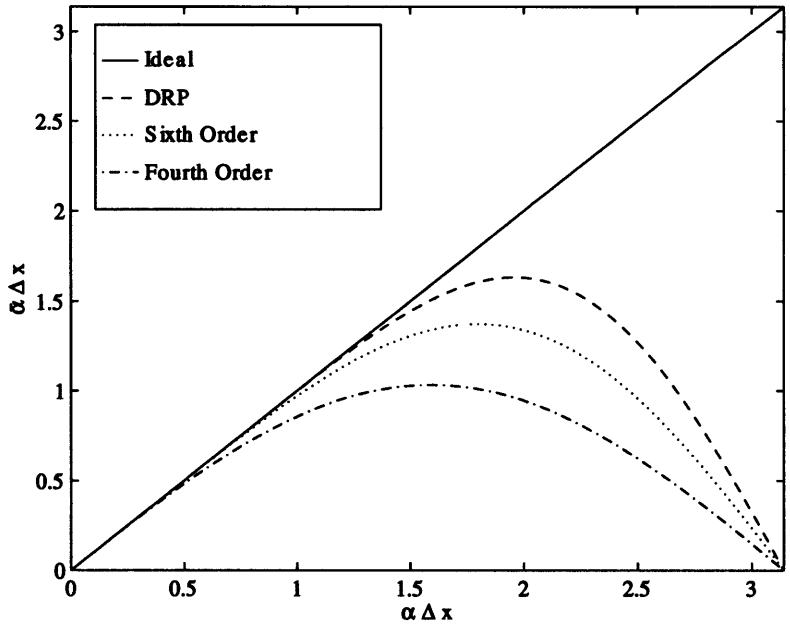

Figure 3.2: Comparison of DRP scheme with fourth and sixth order accurate scheme.

The variable Θ_o represents the wave number range the error function is to be minimized over $(-\pi < \Theta < \pi)$. Choosing $N = 3$ and $\Theta_o = 1$ gives a fourth order accurate scheme. Since this scheme has seven points it can also be compared to a sixth order accurate scheme. From Figure 3.2 the DRP scheme has an improved range of accuracy compared to both the fourth and sixth order standard schemes. The DRP scheme also has improved accuracy in wave propagation speed.

The time discretization is formulated in a very similar way to the space derivatives, except a Laplace transform is taken instead of a Fourier transform. In construction of the higher order method, data from more than one previous time is used to update the current time step. In this formulation, values of time derivatives from previous time steps are used to update the current time step. These values come from the evaluation of space derivatives and any source terms. The time derivative can thus be written as

$$\frac{U^{(n+1)} - U^{(n)}}{\Delta t} \simeq \sum_{j=0}^{N} b_j \left(\frac{dU}{dt}\right)^{(n-j)} \tag{3.14}$$

Taking the Laplace transform of this equation yields

$$\frac{\imath(e^{\imath\omega\Delta t}-1)}{\imath\Delta t\sum_{j=0}Nb_je^{\jmath\omega\Delta t}}\tilde{U}\simeq\frac{d\tilde{U}}{dt}=-\imath\omega\tilde{U}. \tag{3.15}$$

From this a numerical approximation to the ideal variable ω can be defined as

$$\bar{\omega}\Delta t\equiv\frac{\imath(e^{\imath\omega\Delta t}-1)}{\sum_{j=0}^{N}b_je^{\imath j\omega\Delta t}}\simeq\omega\Delta t \tag{3.16}$$

As with the spatial discretization, the numerical approximation $\bar{\omega}\Delta t$ can be optimized with respect to $\omega\Delta t$. The error function E is defined as

$$E=\int_0^{\Theta_o}\{\sigma[\Re(\bar{\omega}\Delta t-\omega\Delta t)]^2+(1-\sigma)[\Im(\bar{\omega}\Delta t-\omega\Delta t)]^2\}d(\omega\Delta t) \tag{3.17}$$

The variable σ is used as a weighting factor between the wave propagation characteristics (real part) and the dissipation (imaginary part).

As with any high order method, the presence of high frequency waves in the solution is a concern. The DRP method is not subject to odd-even decoupling; it does capture unwanted high frequency waves. These waves are easily created at interfaces with solid surfaces and inlet/exit boundaries. The method used for damping is similar in construction to the method used to approximate the space derivatives. The artificial damping used takes the form

$$U_i^{(n+1)}-U_i^{(n)}=\mu_o\sum_{j=-N}^{M}c_jU_{i+j}^{(n)}$$

The variable μ_o is a constant used to adjust the amount of damping. The method chosen for this solver was to evaluate the fourth derivative of pressure at each point and use that value to scale μ_o. This method proved very effective in selecting and removing unwanted high frequency waves from the numerical solution without providing excessive damping of the desired waves.

3.2.2 Gridding Methods

For this solver multiple overlapping grids are used. The flow can be thought of as containing two unique regions: flow about the blades and the flow in the upstream and downstream ducts. These regions have distinct geometries and different flow characteristics. Flow in the duct is governed almost exclusively by the Euler equations. Since the grid is a simple rectangular shape, a simple rectangular(H) grid is used to simplify computation in this region. In fact the geometry is so simple, that the grid lines are able to coincide exactly with the coordinate directions.

Near the blade surfaces viscous forces become very important to appropriately describing the flowfield. Therefore in this region the grid should conform to the blade. In this region a circular(O) grid is used with closely packed spacing near the surface and greater spacing farther away from the blade. Grid orthogonality near the surface is also important. Because of the use of multiple grids a grid interpolation scheme is necessary to pass glow information from one grid to another. Interpolation is necessary because the O and H grids share no common boundaries.

Formulating boundary conditions at the inlet and exit of an unsteady flowfield is challenging. The goal is to allow the interior portion of the flow solver to 'feel' as if the boundaries are very far away. This is particularly difficult in unsteady flows. Simply placing the inlet and exit boundaries far apart is unacceptable due to the long time required for this large domain to react to any unsteady behavior. The linearized Euler equation, which is solved over the H grid, has four possible eigenmodes which specify the flow solution. Along with these eigenmodes are their associated eigenvalues which determine the direction information in the eigenmodes travel. The goal of non-reflecting boundary conditions is to allow all outgoing eigenmodes to leave without generating any incoming modes. This solver uses the approximate unsteady method as described by Giles [1].

Chapter 4

Inviscid Flow Response

To gain a basic understanding of the flow physics, the problem of a density gradient convecting over a blade row is first investigated by looking at this unsteady problem in an incompressible, inviscid flowfield. Knowledge of the basic flow physics will serve as a building block toward compressible and viscous flows. This section details the effects of a single density gradient convecting over a compressor blade row in an inviscid, incompressible flowfield.

4.1 Introduction

The effect of a convecting density distortion on an inviscid, incompressible blade row was investigated by running a series of computational experiments. The density disturbance used for this study is a planar disturbance(normal to the blade row) which varies for freestream density (ρ_1) to a peak density (ρ_2) and back to freestream density(see figure 1.1). Two forms of density variation are studied: a sinusoidal density variation and a flat top density change (see figure 4.1). The sinusoidal wake has a $(1-\sin(\frac{U_\infty \pi t}{w}))$ distribution, so there are no sharp changes in the density distribution of the wake. The 'flat top' also has this type of density change. The flat top changes density sinusoidally over a width of $\frac{w}{c} = 0.05$ at the leading and trailing section of the wake.

Besides a change in the form of the density variation, several basic parameters are

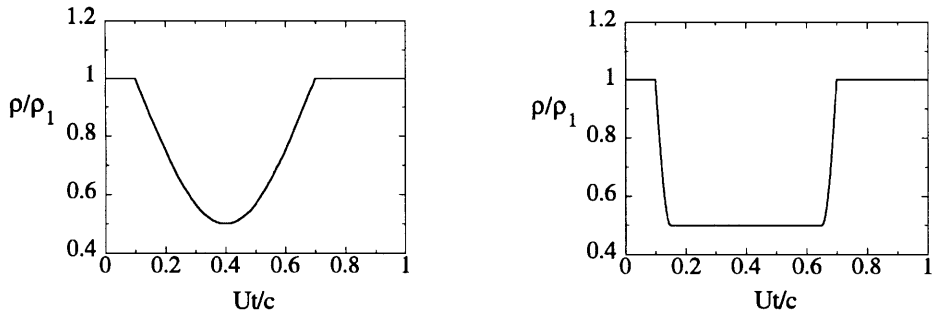

Figure 4.1: Density variation over time for one density distortion. Sinusoidal density change(a) and flat top density change(b) go from free stream density(ρ_1 to peak density ρ_2 and return to free stream ρ_1.

varied. These parameters include: blade geometry, magnitude of density change, and width of density distortion entering the passage. For these tests two blade shapes are studied(see figure 4.2). One blade, referred to as the EEE blade(see figure 4.2a), is highly loaded and has a fairly uniform pressure distribution. The other blade, referred to here as NACA4F(see figure 4.2b), has a lower loading with most of the pressure change occurring over the front half of the blade. All tests were run with flow at incidence to these blades.

Only one density wake convects through the passage for this investigation. Most tests were performed on the NACA4F blades; only four tests were run with the EEE blade row, all with sinusoidal density variations. The parameters for these tests are a density parameter ρ^*, defined as $(\frac{\rho_2-\rho_1}{\rho_1+\rho_2})$, and wake width $(\frac{w}{c})$ where c, the chord length, non-dimensionalizes the width w of the wake. The tests for the EEE blade include

1. $\rho^* = -\frac{2}{3}$ with $\frac{w}{c} = 0.1$
2. $\rho^* = -\frac{1}{3}$ with $\frac{w}{c} = 0.1$ and 0.2
3. $\rho^* = \frac{1}{6}$ with $\frac{w}{c} = 0.2$

Various tests were run on the NACA4F blade. Table 4.1 show the test matrix for sinusoidal wakes encountering this blade shape. Flat top distortions were also run

$\frac{w}{c}$	ρ^*
0.1	$-\frac{2}{3}, -\frac{1}{3}, -\frac{1}{6}, \frac{1}{9}, \frac{1}{6}, \frac{1}{3}$
0.2	$-\frac{1}{3}, \frac{1}{9}, \frac{1}{6}$
0.4	$-\frac{2}{3}, -\frac{1}{3}, -\frac{1}{9}, \frac{1}{9}, \frac{1}{6}, \frac{1}{3}$
0.6	$\frac{1}{9}$

Table 4.1: Table of test matrix

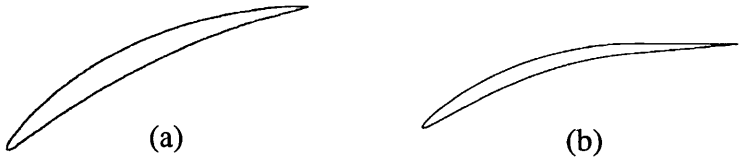

Figure 4.2: Blade geometries used for numerical experiments: EEE blade(a) with blade loading $\psi \approx 0.5$ and NACA4F blade(b) with $\psi \approx 0.31$.

with the NACA4F blade row, all with the same density change and density gradient. Five widths for the flat portion of this distortion are examined. As a starting point, a width of zero is used which compares with sinusoidal tests. The other variations include widths of 0.2,0.6, 0.8, 1.3, and 1.6 chord lengths. Thus the factors affecting loading are not only the width and strength of the density wake, but also blade loading and the form of the density change.

Before continuing with results of the experiments, the general physics of the flowfield will be reviewed. For this explanation a wake with a density deficit will be considered. As the wake approaches the blade row, the density distortion interacts with the blade row pressure field because the density gradient is nearly normal to a pressure gradient. This interaction creates added vorticity in the flowfield (see section 1.2 for more detailed explanation). As the wake encounters the leading edge, a downwash is induced on the blade reducing the blade angle of attack. As the wake passes midchord, an upwash is induced on the blade which causes an increase in angle of attack. This translates into a decrease then an increase in lift. For a wake of higher density relative to free stream the opposite will occur. As the wake encounters the

blade row an upwash will be produced, followed by a downwash as the wake passes mid-chord on the blades. So for a wake with higher density, the lift will increase then decrease to freestream value as the wake leaves the blade row.

4.2 Evolution of Density Wake

The density disturbance is introduced at the inlet to the computational domain($\frac{x}{c} = -0.35$) and convects with freestream velocity U_∞. As the density disturbance encounters the blade row it interacts with the blade pressure gradient, causing a local change in velocity which alters the shape of the density disturbance as it flows through the passage. As the density disturbance enters the blade passage it immediately reacts with the blade pressure gradient. This reaction, as described in section 1.2 results in lower density flow migrating toward the low pressure(suction) side of the blade and the higher density flow moving toward the high pressure side of the blade row. This causes a change in wake shape from a planar disturbance to a more irregular shaped distortion.

As the density wake convects through the passage, the disturbance density will migrate toward one side of the blade row. Upon encountering the blade row the density wake is cut by the blade row, just as a pressure wake would be [4]. An example with $\rho^* = -\frac{1}{3}$ and $\frac{w}{c} = 0.2$ is shown in the plots of constant density in figures 4.3, 4.4, and 4.5. Time for these inviscid tests is normalized so that $t = 0$ corresponds to the wake encountering the leading edge of the blade row. Figure 4.3 shows the density wake at a time $t = 0.15$, corresponding to a midpassage position of the front of the wake of about $\frac{x}{c} = 0.15$ where $\frac{x}{c} = 0$ is the leading edge of the blade. The blade row has cut the density wake, but the wake still has its planar shape. Figure 4.4 shows the wake at a later time $t = 0.65$ when the front of the wake at midpassage is at approximately $\frac{x}{c} = 0.75$. At this point the density distortion has been altered due to equilibrium conditions in the passage. The low density fluid in the wake is traveling toward the suction side of the blade, causing a larger concentration of low density fluid on the suction side. The wake has left the trailing edge of the

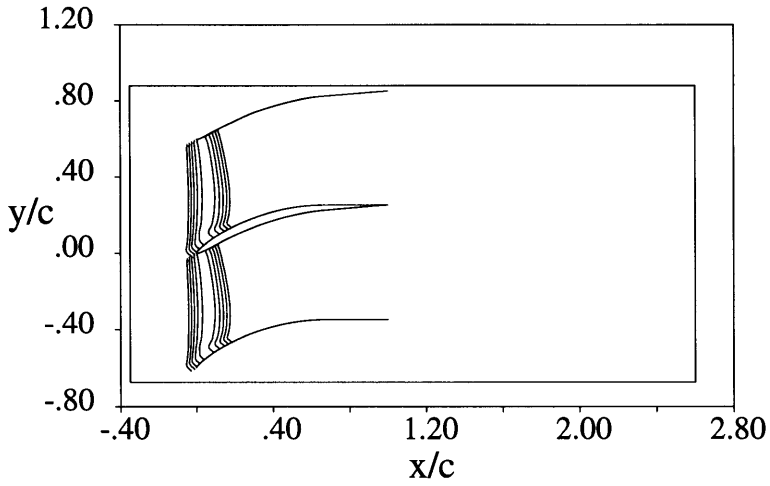

Figure 4.3: Plot of constant density showing position of the density disturbance at $t = 0.15$ where the disturbance is defined by $\rho^* = -\frac{1}{3}$ and $\frac{w}{c} = 0.2$.

blade row in figure 4.5. This corresponds to a time of $t = 1.15$ and a midpassage position of the front of the wake of $\frac{x}{c} = 1.28$. The planar wake has distorted during its passage through the blade row. The wake has a thinner width at the pressure side of the blade row and a larger concentration of low density fluid at the suction side of the blade row.

A larger density gradient (smaller width for given ρ^*) causes the wake to deform more quickly because a higher gradient creates more added vorticity, and thus greater circumferential velocity to transport the density toward one side of the blade. The low density disturbance changes from a planar wake to a blob of non-uniform density as it leaves the blade passage. A wake with a density increase reacts similarly except that the flow migrates toward the pressure side of the blade row and not the suction side. Thus as the density wake flows to the next blade row, its shape is no longer planar. The blade row pressure field changes the shape of density disturbances as they convect through the passage. The pressure difference in the passage has the effect of forcing the lower density fluid to the low pressure side of the passage to achieve equilibrium. This creates a concentrated mass of nonuniform density exiting the blade row. The form of a density wake entering a downstream blade row is thus greatly altered.

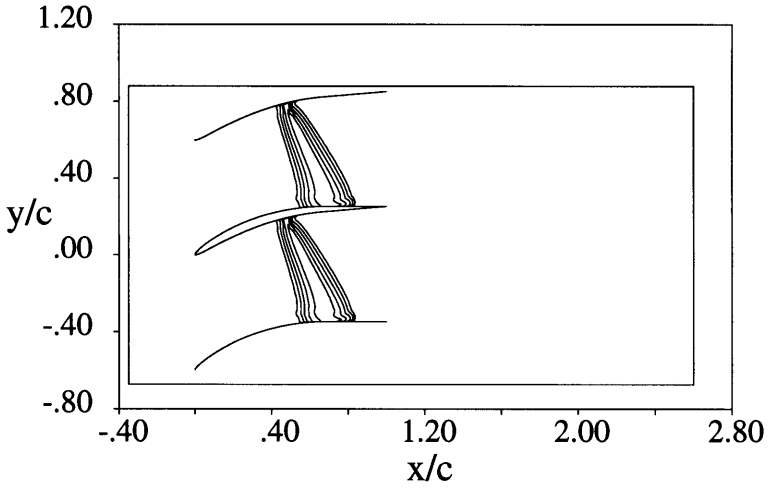

Figure 4.4: Plot of constant density showing position of density disturbance at $t = 0.65$ where the disturbance is defined by $\rho^* = -\frac{1}{3}$ and $\frac{w}{c} = 0.2$.

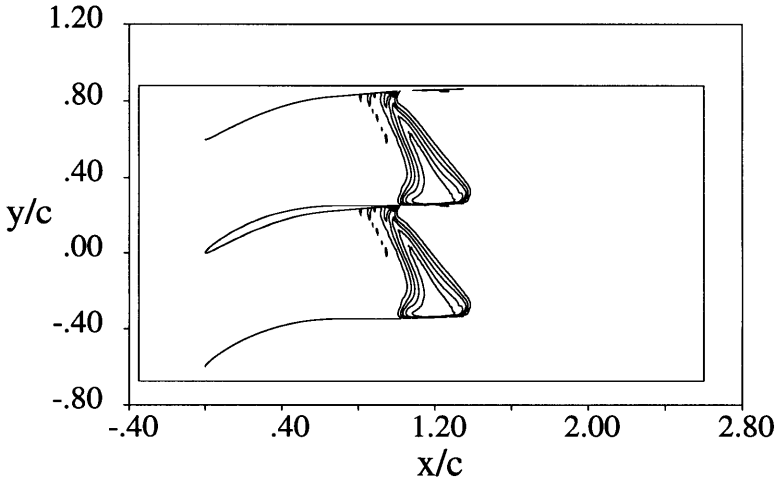

Figure 4.5: Plot of constant density showing position of density disturbance at $t = 1.15$ where the disturbance is defined by $\rho^* = -\frac{1}{3}$ and $\frac{w}{c} = 0.2$.

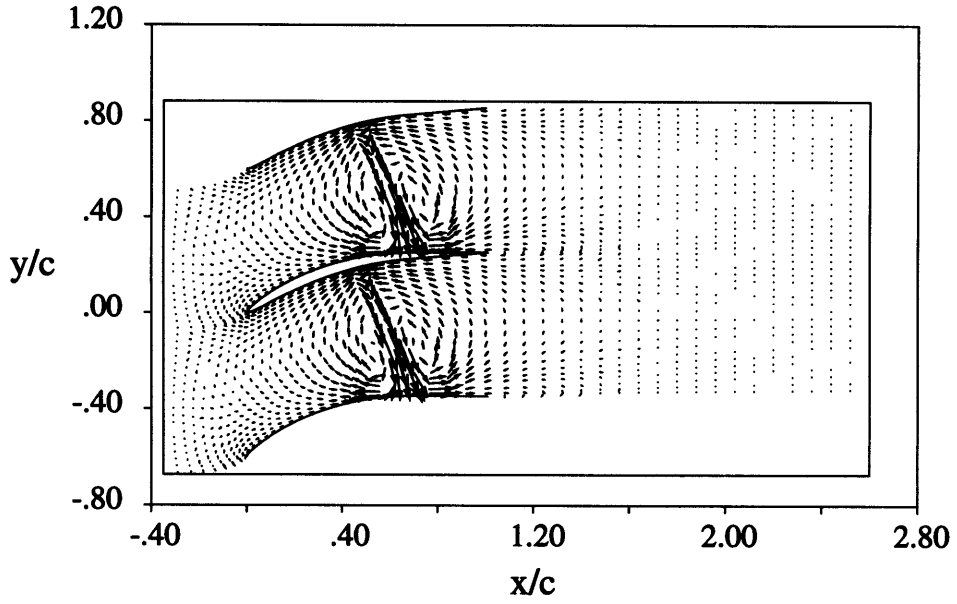

Figure 4.6: Disturbance velocity vectors for sinusoidal density wake with $\rho^* = -\frac{1}{3}$ and $\frac{w}{c} = 0.2$ at time $t = 1.0$

4.3 Induced Vorticity

A clear understanding of the changes in loading can be obtained by examining the disturbance velocity field. For this purpose the density wake examined in figure 4.4 is studied. To conform with compressor nomenclature, the 'x' direction from the figure is referred to as the axial direction, and the 'y' direction is referred to as the circumferential direction. The test case in figure 4.4 involves convection of a sinusoidal wake convecting over the NACA4F blade row. The density wake has a strength $\rho^* = -\frac{1}{3}$ and a width of $\frac{w}{c} = 0.2$. A density deficit causes a downwash as the wake encounters the blade and an upwash as the wake passes midchord. As the density distortion encounters the blade row, counterrotating vorticies are formed along the density distortion. These vorticies can be clearly seen by examining the disturbance velocity vectors, (see figure 4.6). In this figure the wake has convected $t = 0.15$, corresponding to the wake position as seen in figure 4.4. At the center of the wake where the density peak negative circumferential velocity is formed(see figure 4.6). This translates into a force in the negative circumferential direction, causing a reduction in angle of attack and therefore a reduction in lift. As the velocity

perturbation travels to the back half of the blade, the negative circumferential velocity translates into an increase in blade angle of attack and thus an increase in lift. This varying force gives an unsteady moment on the blade. The unsteady moments for this study are calculated about midchord. The downward velocity created as the wake convects through the passage creates a counterclockwise moment as the wake convects over the first half of the blade and a clockwise moment as the wake travels over the back half of the blade. Therefore the time varying moment will increase then decrease to freestream value when the wake is at the midchord. The moment will decrease farther and then increase to freestream as the wake leaves the trailing edge.

These disturbance flowfields also indicate how parametric changes affect blade loading. Changes in the wake parameters alter the added vorticity in the flowfield. The three parameters which define the wake are the distribution of the density change, the strength of the density wake(ρ^*), and the width of the wake($\frac{w}{c}$). Two wake shapes are examined, a sinusoidally varying density change and the flat top density change(figure 4.1). Two wakes with the same width and strength but different distributions will have very different effects on the flowfield. The flat top wake has a higher density gradient because the density change occurs over a much smaller length. A higher density gradient means that more vorticity is created, from the vorticity equation

$$\frac{D\omega}{Dt} = -\frac{1}{\rho^2}(\nabla\rho \times \nabla p) \tag{4.1}$$

So a flat top has a higher density gradient and thus creates more added vorticity in the blade row. This is clearly illustrated in figures 4.7 and 4.8 where a sinusoidal and flat top wake have convected through the passage, creating added vorticity and thus a disturbance velocity field. Both wakes have a strength $\rho^* = \frac{1}{9}$ and a width $\frac{w}{c} = 0.6$. The wakes have traveled the same distance as those in figure 4.4, but are three times as wide. Because the density parameter is smaller in magnitude these disturbance fields are scaled to three times those of figure 4.6 to make the disturbance vectors more visible. Each wake creates counterrotating vorticies because the density first increases then decreases. The centers of these vorticies are farther apart for the flat

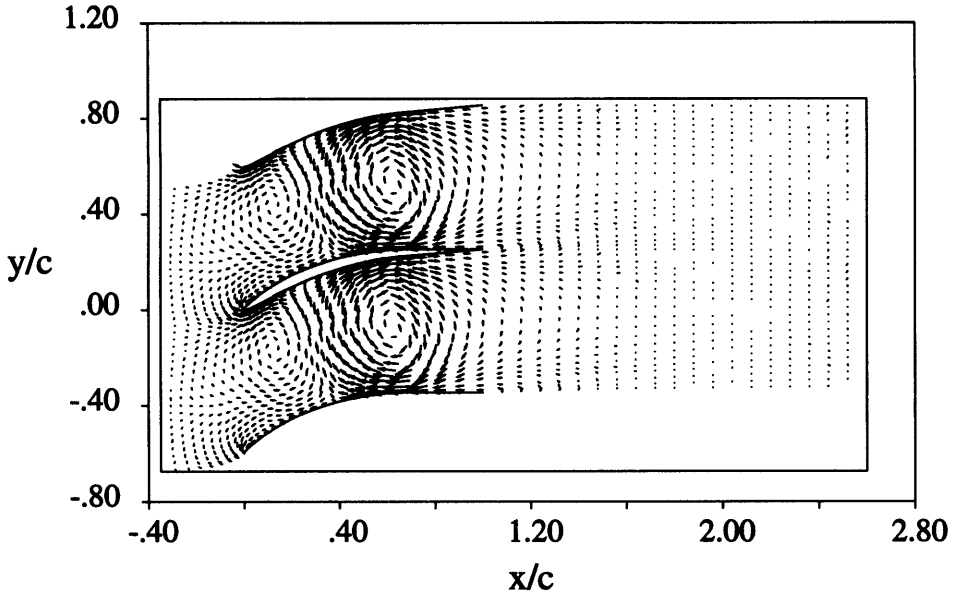

Figure 4.7: Disturbance velocity vectors for sinusoidal density wake with $\rho^* = \frac{1}{6}$ and $\frac{w}{c} = 0.6$ at time $t = 2.0$.

top wake. This changes the time scale between the two wake shapes. The flat top wake loading changes faster because the center of the first flat top vortex has traveled farther than the sinusoidal wake vortex for the same convective time. The peak in loading will occur at the same time for the wakes because the wakes are of the same width.

The added vorticity in the passage is also dependent upon the strength of the wake. The magnitude of density change determines the magnitude of the vorticity. For a constant wake width an increase in the magnitude of the strength(ρ^*) of the wake will increase the vorticity. Also a change in the sign of the strength(density deficit or increase) will change the orientation of the vorticies(see figures 4.6 and 4.7). The width of the wakes determines the distance between the centers of the counterrotating vorticies. Thus for larger wakes the vorticies will be farther apart and will not have as strong an influence on each other.

The density distortions are defined by their strength(ρ^*), width($\frac{w}{c}$), and density distribution. These parameters directly relate to the changes in vorticity. Any change which alters the local density gradient will alter the vorticity. This change then

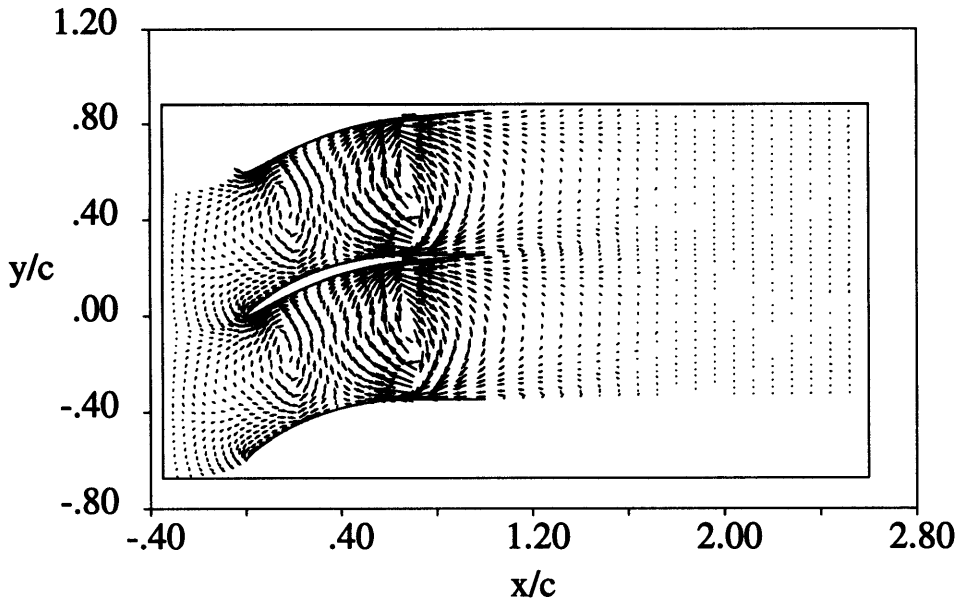

Figure 4.8: Disturbance velocity vectors for flat top wake with $\rho^* = \frac{1}{6}$ and $\frac{w}{c} = 0.6$ at time $t = 2.0$.

translates into a change in the magnitudes of the time varying lift and moment. The change in vorticity also relates to a change in static pressure distribution on the blade. Static pressure changes can then be translated into changes in lift and moment.

4.4 Static Pressure Distributions

The static pressure distribution across a blade row affects the unsteady loading caused by a convecting density wake. The effect of differences in pressure distribution across the blade row directly affects the changes in loading caused by a density wake. The two blades studied, the EEE blade and the NACA4F blade, have very different pressure distributions. Figures 4.9 and 4.10 show the difference in static pressure coefficient across the blades as a sinusoidal wake with $\rho^* = -\frac{1}{3}$ and $\frac{w}{c} = 0.2$ convects through the passage. Both figures show the static pressure difference across the blade row, starting just aft of the leading edge of the blades. The steady state pressure distribution is represented at *time* $= -0.35$, before the wake enters the passage. The EEE blade has an even pressure loading, but the NACA4F blade is forward loaded. The trailing

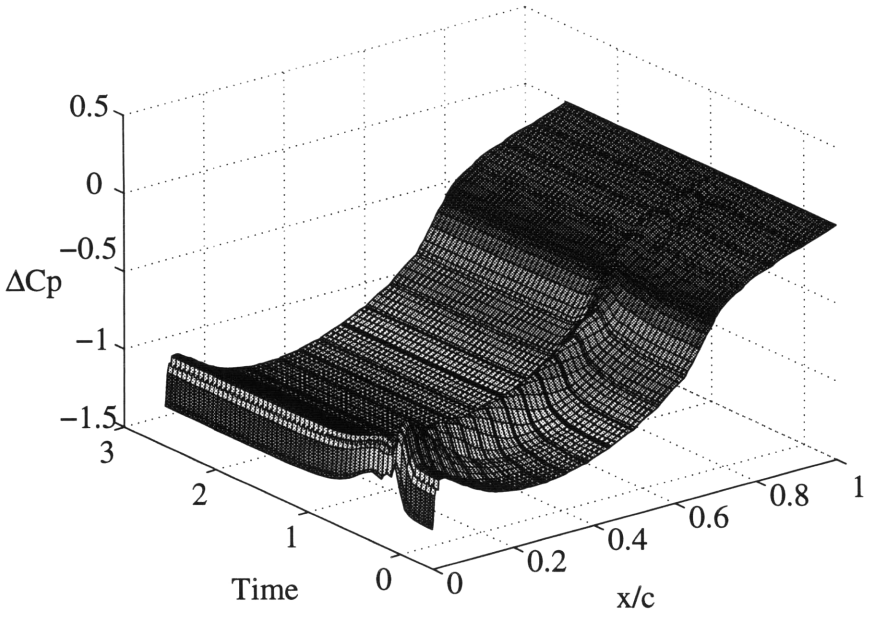

Figure 4.9: ΔCp distribution for NACA4F blade row with convecting sinusoidal density wake of strength $\rho^* = -\frac{1}{3}$ and $\frac{w}{c} = 0.2$. The blade chord ranges from $0 \leq \frac{x}{c} \leq 1$;the wake encounters the blade row at $Time = 0$ and leaves at $Time = 1$.

edge of the NACA4F blade has very loading. From the vorticity equation (see equation 4.1), baroclinic torque will scale with pressure gradient. Because the pressure gradients are different, the vorticity formation and thus the changes in blade loading will be different. As the wake convects through the blade row, the added vorticity in the passage causes a sinusoidal bump in the pressure coefficient which travels along the blade. This sinusoidal 'bump' corresponds with the sinusoidal density change; the shape of the pressure bump corresponds with the shape of the density gradient. As the wake encounters the second half of the NACA4F blade, the magnitude of this bump decreases because the pressure gradient has decreased. Thus the magnitude of the change in loading on the blade row scales with the magnitude of the pressure difference across the blade.

The unsteady change in the pressure coefficient is seen as a 'bump' as the wake traverses the blade row. From figures 4.9 and 4.10 this bump has a sinusoidal shape because the wake has a sinusoidal density gradient. This bump will always have a shape similar to the wake, and will be a bump or a recession depending on whether the

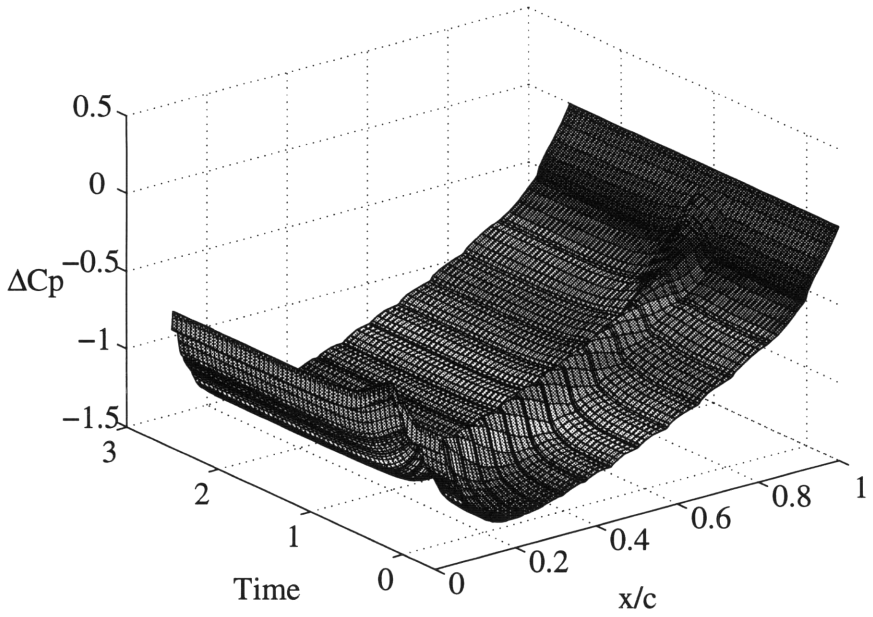

Figure 4.10: ΔCp distribution for EEE blade row with convecting sinusoidal density wake of strength $\rho^* = \frac{1}{3}$ and $\frac{w}{c} = 0.2$. The blade chord ranges from $0 \leq \frac{x}{c} \leq 1$; the wake encounters the blade row at $Time = 0$ and leaves at $Time = 1$.

wake is an increase or a decrease in density. Figure 4.11 shows the pressure coefficient for the NACA4F blade row as a flat top wake of strength $\rho^* = \frac{1}{9}$ and width $\frac{w}{c} = 0.6$ convects over the blade row. The density change is an increase, so the 'bump' in the pressure distribution is recessed. This bump has a similar shape to the shape of the density change, but is slightly sinusoidal because of the total pressure difference across the wake. The higher total pressure outside the wake compresses the wake slightly so the density change is more sinusoidally, and there are no sharp variations. The time varying pressure change clearly shows the form of the wake as it traverses through the passage, and shows the magnitude of change compared with the steady state static pressure difference.

4.5 Lift and Moment

Because the density wake causes added vorticity in the flowfield, the blade feels a time varying lift and moment. As the density wake enters the blade passage an additional vorticity is formed. For a low density wake, as the wake travels over the front of

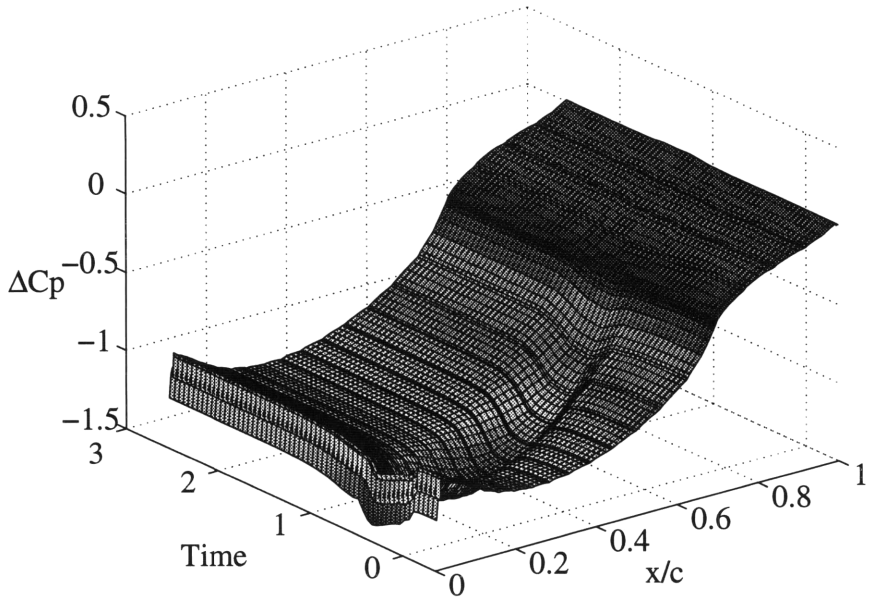

Figure 4.11: ΔCp distribution for NACA4F blade row with convecting flat top density wake of strength $\rho^* = \frac{1}{6}$ and $\frac{w}{c} = 0.6$. The blade chord ranges from $0 \leq \frac{x}{c} \leq 1$; the wake encounters the blade row at $Time = 0$ and leaves at $Time = 1$.

the blade a downwash is produced which reduces the local angle of attack. The lift thus decreases until the wake passes the center of pressure of the blade. The added vorticity will then cause an upwash, corresponding to an increase in the local angle of attack and thus and increase in lift. As the density wake travels through the blade passage, the blade first experiences a decrease in lift then an increase again returning to the steady state value as the wake leaves the trailing edge of the blade. The initial downwash on the blade causes a counterclockwise moment. The upwash then causes a clockwise moment. So the moment will increase, return to steady state at the center of pressure, decrease, then return again to steady state. Figure 4.12 shows time varying lift and moment for a sinusoidal density wake of strength ($\rho^* = -\frac{1}{3}$) and width $\frac{w}{c} = 0.2$ convecting over the NACA4F blade row. In figure 4.12 a slight bump on the lift and moment curves occurs as the back of the wake convects over the leading edge of the blade, at about $Time = 0.1$. The bump occurs for small wake widths ($\frac{w}{c} < 0.4$), and its presence is not dependent upon the gradient of the density. The bump will occur for even small gradients as long as the wake width

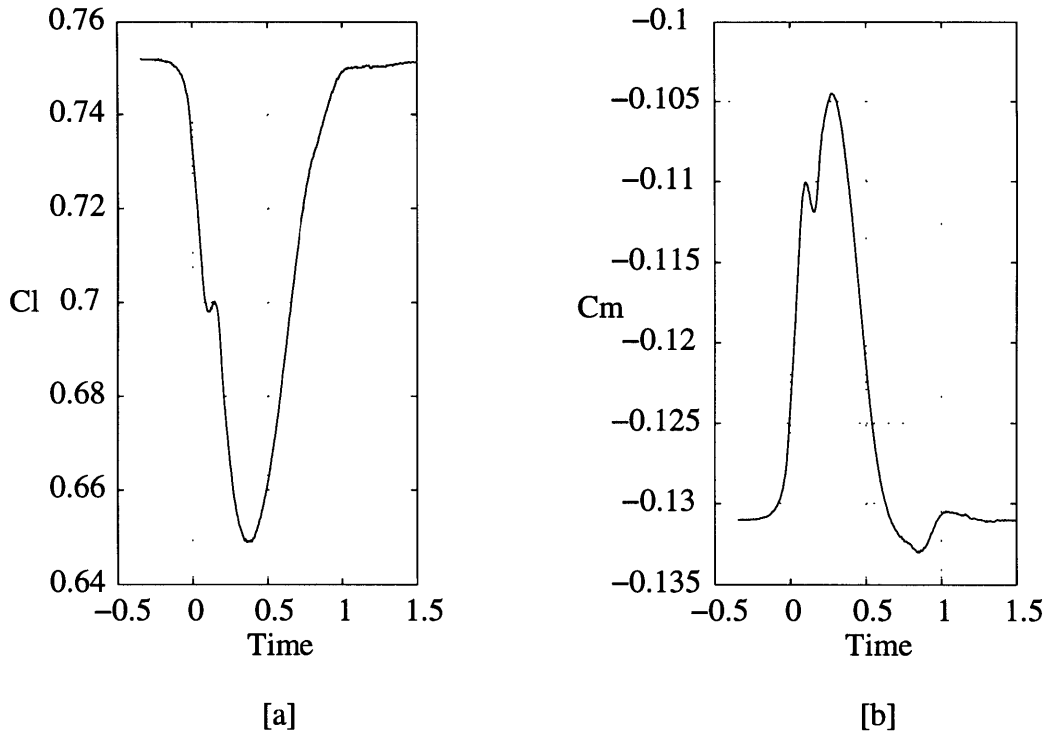

Figure 4.12: Example of lift (a) and moment (b) for NACA4F blade with sinusoidal wake of strength $\rho^* = -\frac{1}{3}$ and $\frac{w}{c} = 0.2$. The lift changes 13% and the moment changes by 20%.

is small, gradually becoming less prominent as the width is increased. The density gradient is important to the size of the bump; for larger gradients the magnitude of the bump can exceed that of the peak due to the interaction between pressure and density gradients. This effect is not seen at the trailing edge for the NACA4F blade because the blade has very little loading at the trailing edge. This effect is second order and will not be examined further in this investigation. The change in loading due to the interaction of the pressure and density gradients is influenced by the blade geometry and the wake characteristics.

4.5.1 Blade Passage Geometry

Blade geometry influences the change in blade loading due to a convecting density disturbance. The blades used for this study, the NACA4F blade and the EEE blade, have different blade loadings and different loading distributions(see figure 4.2). The

difference in blade loadings is a major factor for the changes in lift; the changes in moment are dependent upon the blade loading, passage pressure rise, and blade loading distribution.

The convecting density wake causes a time varying lift which peaks as the wake reaches midchord and returns to steady state as the wake leaves the trailing edge of the blade(see figure 4.12). The time scale for different blades is similar but not quite identical because the axial velocity in the passage is slightly different for each blade, but not largely different compared with the freestream velocity. The magnitude of change for different blades is dependent upon the steady state lift values. For the two blade geometries with the same convecting density wake, the change in lift curves scale directly with the steady lift. So the parameter $\frac{\Delta Cl}{Cl_{steady}}$ will give blade independent lift information.

The time varying moments again have similar time scales, with slight differences because of passage axial velocities. The moment is not only dependent upon the blade loadings, but also the loading distribution. From figure 4.12 with moment taken about $\frac{x}{c} = 0.5$, the positive change in moment is greater than the negative change in moment because the front of the blade is more heavily loaded than the back of the blade. This occurs because the change in vorticity scales with the pressure gradient, see equation 4.1. Thus a stronger moment is created as the wake passes the front of the blade than when the wake passes the back of the blade. The EEE blade has a more even pressure distribution so the change in moment as the wake passes the trailing portion of the blade will be larger. Comparing the varying moments of the different blades is more complicated than it was for the lift. The changing moment cannot simply be normalized by the steady state moments because the loading across the passage will also have an effect. The moment can be normalized by the steady moment and the blade passage pressure rise, so that the parameter $\frac{\Delta Cm}{\psi Cm_{steady}}$ gives blade independent moment information.

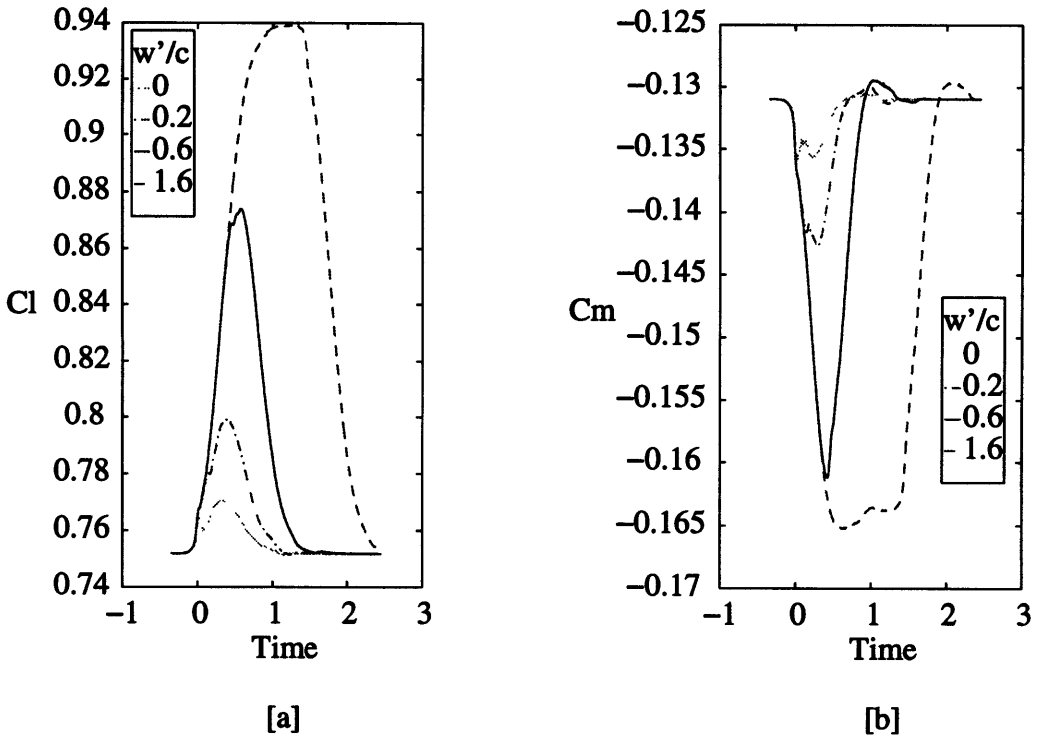

Figure 4.13: Time varying lift(a) and moment(b) caused by flat top density wakes convecting over the NACA4F blade row. The width $\frac{w'}{c}$ is the width of the flat portion of the wake.

4.5.2 Flat Top Results

The flat top test series is a derivative of the sinusoidal tests. The flat top is simply a sinusoidal change with a period of peak density flow. For these tests a density change of $\rho^* = \frac{1}{9}$ is used. The flat top wake tests indicate the distance between density gradients needed to reach an interim steady state solution at which time the interim force equals the previous force scaled by the ratio of the densities($\frac{\rho_2}{\rho_1}$). Four test cases for the flat top wakes are shown in figure 4.13, the other widths tested include $\frac{w}{c} = 0.8, 1.3$. The legend shows the distance($\frac{w'}{c}$) of flat space in the wake. The wakes have a sinusoidal gradient of width $\frac{w}{c} = 0.05$ on either side. This means the case with zero flat top corresponds with a sinusoidal wake of width $\frac{w}{c} = 0.2$. All flat top tests were run using the NACA4F blade row.

Because all of the tests have the same density gradient, the slope for the change in loading is the same between test cases. From [a] of figure 4.13 the magnitude of

the lift will increase as the flat top width increases, until reaching steady state at a flat width just over one chord length. The interim steady state is just over one chord length because at a width of one chord length the back of the wake will interact with the upstream potential of the blade row. The peak values for the lift increase linearly until the width becomes close to one chord length. The same is not true for the moment because the moment has a different time scale. The peak moment is reached for a flat top width beginning at about $\frac{w}{c} = 0.8$, but this is not the interim steady value. This moment peak is an overshoot. From [b] of figure 4.13 the moment for a a width of $\frac{w}{c} = 1.3$ overshoots the interim value, returns to the interim steady state as the density gradient leaves the trailing edge of the blade, then increases again to steady state. More tests are be needed to determine the rate of moment increase until the interim steady state is reached.

For a density wake with a gap of constant density, interim steady state solutions are reached at just over one chord length for both the lift and the moment. The magnitude of the lift increases nearly linearly toward this interim value, but the moment does not. The moment approaches the interim value faster than the lift, but overshoots the interim value. The interim value is reached at about one chord length but the overshoot value is achieved at less than one chord length of constant density. This gives an estimate of the loading for variations of the sinusoidal case if the sinusoidal case is known.

4.5.3 Sinusoidal Results

Several sinusoidal test cases were run to find scaling parameters which determine the peak changes in loading. Both the NACA4F and EEE blade rows were used for the sinusoidal tests. Wake widths of $\frac{w}{c} = 0.1, 0.2, 0.4$ and density changes of $-\frac{2}{3} \leq \rho^* \leq \frac{1}{3}$ are used for the dimensional scaling. The values of ρ^* typical to compressors are around $\rho^* = 0.1$ while those for turbines are closer to $\rho^* = 0.3$. Larger changes in density(ρ^*) and larger wake widths will give larger changes in lift and moment because larger density changes produce greater vorticity, and larger wake width produces more area for the vorticity to act over.

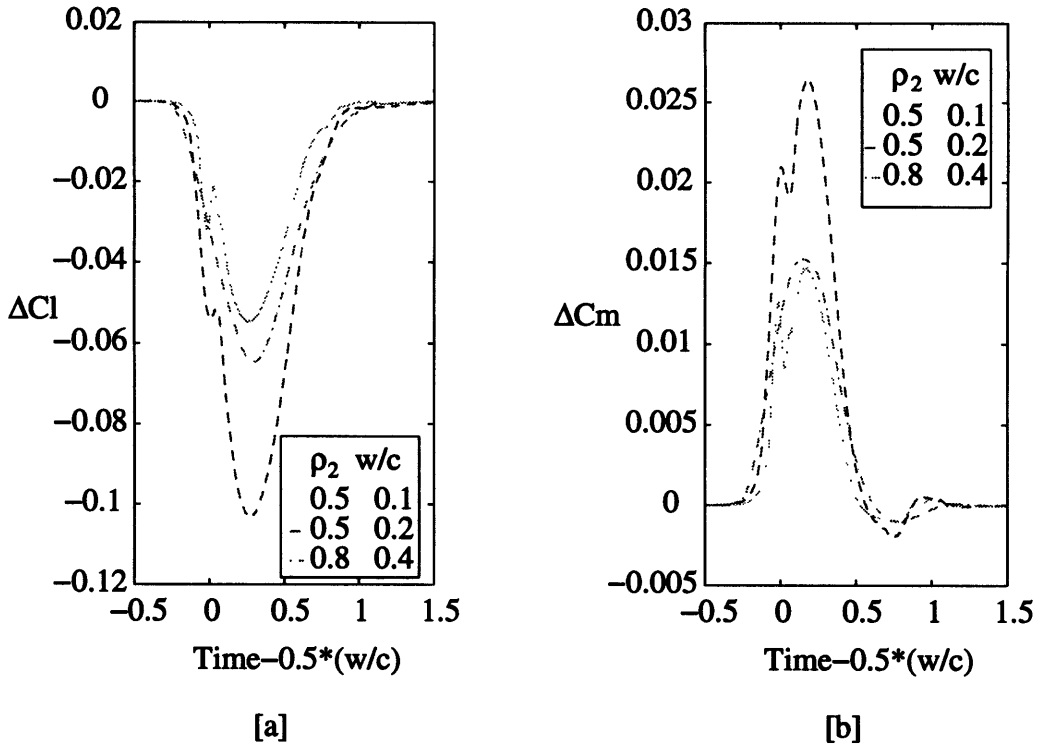

Figure 4.14: Changing lift(a) and moment(b) curves for different wakes versus a time scaling factor based on wake width. Curves have similar shapes for different wake characteristics, so effects of wakes can be compared based on peak values.

The changes in lift and moment will be scaled by looking at the peak change in lift and moment. This can be done because the loading changes all have similar shapes(see figure 4.14). Figure 4.15 shows a plot of the peak change in lift as a function of ρ^*. Three widths are shown: $\frac{w}{c} = 0.1, 0.2, 0.4$. The lines represent second order polynomial curve fits to the data. Because we are using second order computational tools, only two decimal places will be kept. For small values of $(\frac{w}{c})$, the lift scales linearly with ρ^*. For $\frac{w}{c} = 0.4$ the lift still scales linearly for the region of interest for the compressor. This scaling looks like:

$$\frac{\Delta Cl}{Cl_{steady}} = 2.19(\frac{w}{c})\rho^* \tag{4.2}$$

in the linear term. The origin of the constant cannot be completely determined with the data obtained. The moment is also very linear for small widths and for small

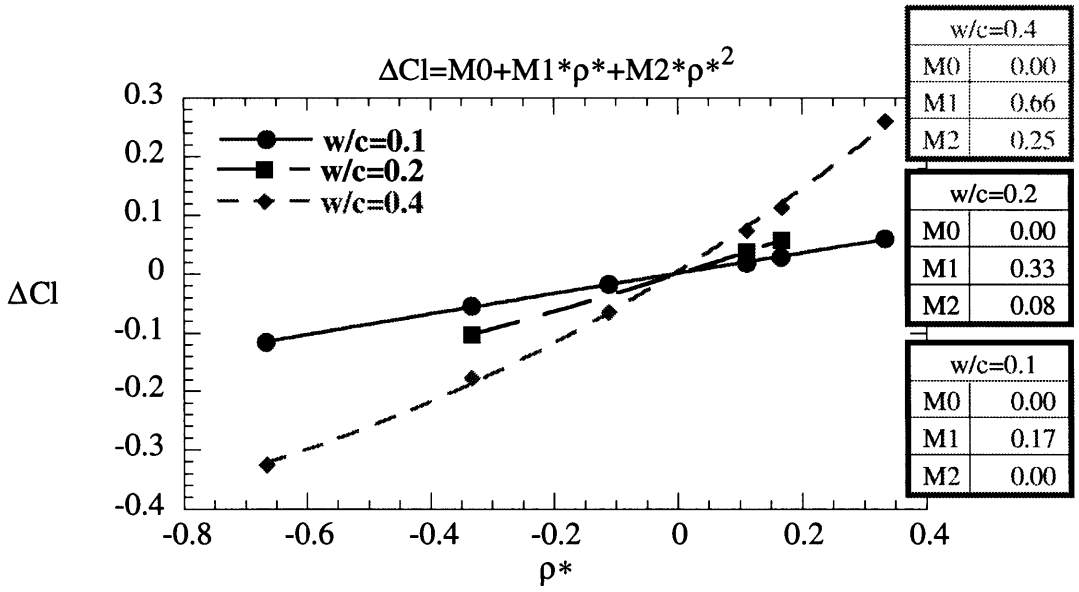

Figure 4.15: Peak of changing lift for tests with sinusoidally varying density wakes convecting through NACA4F blade row.

density changes(see figure 4.16). The linear term for the moment is then

$$\frac{\Delta Cm}{Cm_{steady}} = 3.05(\frac{w}{c})\rho^* \tag{4.3}$$

The nonlinear term for the moment contains an extra length parameter making the change in moment

$$\frac{\Delta Cm}{Cm_{steady}} = 3.05(\frac{w}{c})\rho^*(1 + (\frac{w}{c})\rho^*) \tag{4.4}$$

Thus lift and moment curves for different sinusoidal wakes compare linearly for small wake widths on the NACA4F blade row. For typical compressor density variations of $\rho^* \approx 0.1$ the peaks in both lift and moment scale linearly. This linear response occurs for the NACA4F blade which has linearity in the pressure difference along the blade(ΔCp). For the EEE blade row which has a much stronger pressure difference along the blade the scaling may no longer be linear. The peak lift and moment changes for the EEE blade tests are shown figures 4.17 and 4.18. Only two points for each width $\frac{w}{c} = 0.1, 0.2$ are available. The points do not scale as exactly with ρ^* and $\frac{w}{c}$ as the NACA4F tests do. For the smaller width wake $\frac{w}{c} = 0.1$ the lift and

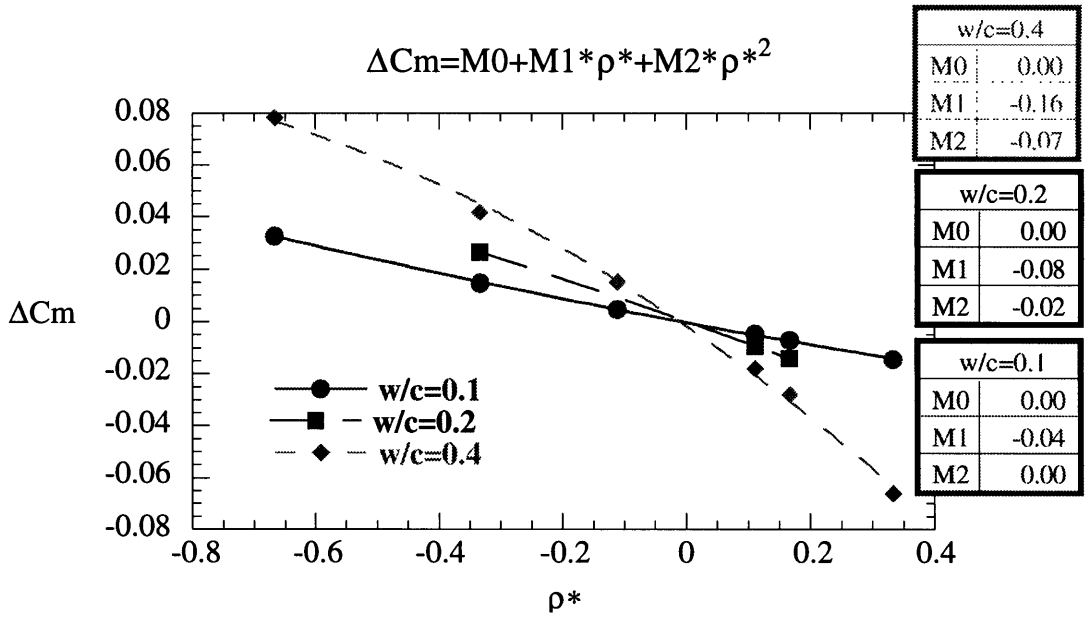

Figure 4.16: Peak of changing moment for tests with sinusoidally varying density wakes convecting through NACA4F blade row.

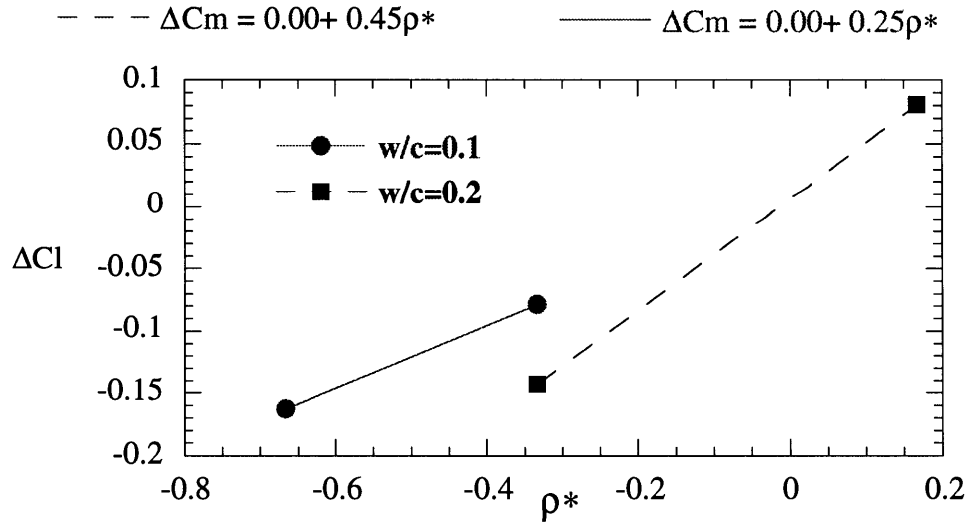

Figure 4.17: Peak of changing lift for tests with sinusoidally varying density wakes convecting through EEE blade row.

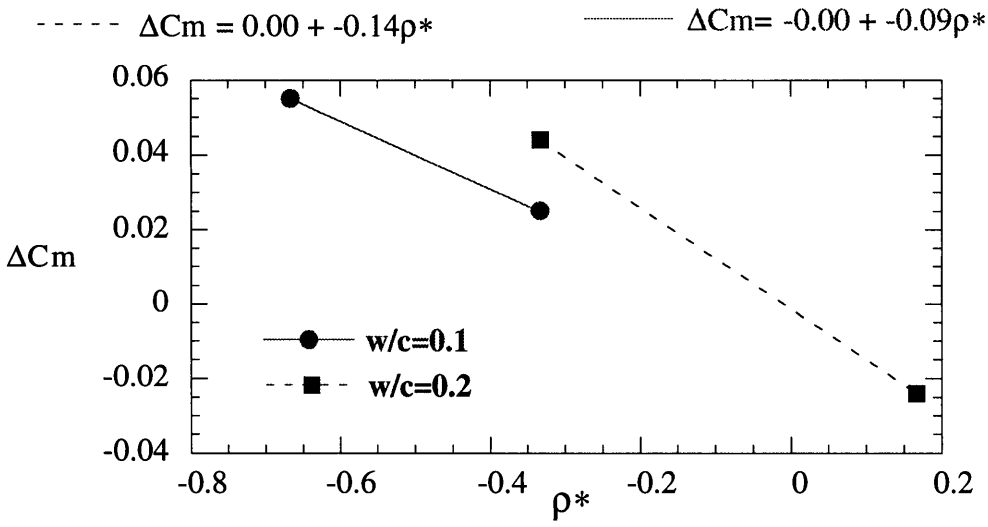

Figure 4.18: Peak of changing moments for tests with sinusoidally varying density wakes convecting through EEE blade row.

moments are

$$\frac{\Delta Cl}{Cl_{steady}} = 2.34(\frac{w}{c})\rho^* \tag{4.5}$$

$$\frac{\Delta Cm}{Cm_{steady}} = 6.45(\frac{w}{c})\rho^* \tag{4.6}$$

The larger width wake does not give quite the same relations as the smaller width, suggesting that some nonlinearity may be present which cannot be determined from the available data. A larger test matrix for these widths may show a stronger tendency toward linearity, or may show nonlinearities occurring because of the strong pressure gradients across the blade row. The larger wake width relations are

$$\frac{\Delta Cl}{Cl_{steady}} = 2.10(\frac{w}{c})\rho^* \tag{4.7}$$

$$\frac{\Delta Cm}{Cm_{steady}} = 5.02(\frac{w}{c})\rho^* \tag{4.8}$$

The lift relations for the EEE blade row look very similar to those for the NACA4F blade, verifying the relations between blade geometries found in section 4.5.1. The constants in the moment relations for different widths are very different. The moment peaks for the NACA4F blade become more nonlinear as the width increases. Therefore

moment peaks for the EEE should not be linear, but the nonlinearities cannot be found with the available data. The constants in the moment relations follow the geometric scaling relations found from section 4.5.1. From the NACA4F blade the moment peak relation when scaled by the blade row pressure rise is

$$\frac{\Delta Cm}{\psi Cm_{steady}} = 9.84(\frac{w}{c})\rho^*(1 + (\frac{w}{c})\rho^*) \tag{4.9}$$

The moment relations for the EEE blade row for widths of $\frac{w}{c} = 0.1$ and 0.2 respectively are

$$\frac{\Delta Cm}{\psi Cm_{steady}} = 12.90(\frac{w}{c})\rho^* \tag{4.10}$$

$$\frac{\Delta Cm}{\psi Cm_{steady}} = 10.04(\frac{w}{c})\rho^* \tag{4.11}$$

Although the linearity of the EEE loading data cannot be verified, the blade and wake comparisons yield very important information. The EEE and NACA4F experiments with convecting sinusoidal wakes show that for blade rows of the same Reynolds number and spacing the following functional relations determine loading changes:

$$\Delta Cl = f(Cl_{steady}, \rho^*, \frac{w}{c}) \tag{4.12}$$

$$\Delta Cm = f(Cm_{steady}, \psi, \rho^*, \frac{w}{c}) \tag{4.13}$$

These parameters give the key scaling parameters. Other factors such as pressure gradient and buoyancy effects may explain differences between the blade loading relations. Besides these key parameters the Reynolds number and blade spacing may contribute to the constant in the lift and moment relations.

4.6 Summary

The inviscid numerical experiments serve as a building block for physical understanding. The vorticity in the passage created by the interaction of the density and pressure gradients act to distort a planar wake and move the nonuniform density toward one

side of the blade. As the wake convects through the passage, this added vorticity creates a time varying lift and moment on the blade. The flat top wake is a variation of a sinusoidal density wake. For large flat top distances the peak change will equal $\frac{\rho_2}{\rho_1}$ times the original loading. As this flat top decreases toward a sinusoidal wake, the change in loading gradually changes to the sinusoidal value. From the sinusoidal density studies, the changes in lift and moment for a given density wake are dependent upon blade geometry. The changes in lift scale with the steady state value of lift for that blade, and the change in moment scales with the blade's steady state value and blade pressure rise. For the sinusoidal density variations in the compressor regime, peak changes in lift and moment have a linear scaling with two wake parameters: ρ^* and $\frac{w}{c}$. The peak changes also scale with blade characteristics: the changing lift scales with steady state lift and the changing moment scales with steady state moment and blade passage pressure rise. This linearity comes from tests on the NACA4F blade, but does not hold equally well for the EEE blade because the NACA4F blade has linearity in the pressure gradient across the blade row. For the cases investigated, changes in loading for different blades and wake characteristics scale linearly in the compressor regime, although further tests should be performed to verify this for highly loaded compressor blade rows. This linearity holds for wake characteristics in the compressor regime but may not hold for highly loaded compressor blades, and certainly not for very nonlinear turbine blades.

Chapter 5

Viscous Flow Response

The inviscid exploration gave an understanding of the basic flow physics. For a real compressor viscosity is important. This chapter outlines an introduction to the effects of viscosity on the convecting density gradient problem. As the density gradient enters the blade row it interacts with the blade pressure gradient to produce vorticity, but it also encounters the blade boundary layer. To amplify the problem for this example, a flowfield with a large boundary layer(near stall conditions) is used.

5.1 Introduction

The effects of a convecting density gradient on the boundary layer of a blade is explored using a finite difference Navier-Stokes code(Hoying, see section 3.2). Due to computational time constraints, only two test cases were run. These tests use the same EEE blade as that used for the inviscid tests, except this blade row is run near stall and at different Reynolds numbers. Both tests use a sinusoidal wake with $\rho^* = -\frac{1}{3}$.

Two test cases were run for the viscous flow solution. Both tests have the same ρ^*, density distribution, and blade configuration. One test case, referred to as test one, has a higher Reynolds number, $1e6$, and a wake width of $\frac{w}{c} = 0.4$. The other test case, test two, has a lower Reynolds number, $698,671$ with a wake width of $\frac{w}{c} = 0.6$. These tests are taken from a nine test Latin squares test matrix [7]. The Reynolds

numbers used in the matrix were chosen assuming that blade response may depend upon the skin friction coefficient. The operating conditions of these tests are too high to run at lower Reynolds numbers. The tests show changes in the boundary layer shape and the boundary layer separation as the density wake convects through the passage.

5.2 Density Wake Evolution

The density wakes for these studies are the same sinusoidal type wakes studied for the inviscid flow investigation. The wake enters the blade passage planar to the blade row. As the wake encounters the blade leading edge it is cut by the blade row just as it was for inviscid flow(see constant density contours of figures 5.1 and 5.2). As the wake convects through the blade row it reacts to the boundary layer. The boundary layer represents a region of slower flow. Because the density wake travels with the local flow velocity, it will be slowed at the blade surfaces. Because of the presence of the boundary layer, the wake will not deform as it did for the inviscid flowfield.

Density contours of figures 5.3 and 5.4 show the density wakes for both test cases after traveling the same distance along the blade. The wakes travel much slower at the blade surface because of the boundary layer. A region of lower density fluid travels very slowly near the surface of the suction side, just before the separation point. The density wake then flows around the boundary layer. This causes the density wake to concentrate in the center of the passage between the boundary layers of the upper and lower blade surface. As the distortions leave the passage (see figures 5.5 and 5.6), they begin to wrap around the back of the boundary layer because the added vorticity in the flowfield causes a velocity disturbance acting downward on the suction side of the blade, just as in the inviscid case of figure 4.6. After leaving the trailing edge of the blade row, the density distortion encounters vorticity shed from the blade row(see figures 5.7 and 5.8). This has the effect of mixing the densities so that no concentration of high or low density fluid exists in the passage. The next blade row will not see a concentrated density distortion. The smaller wake of figure 5.7 is

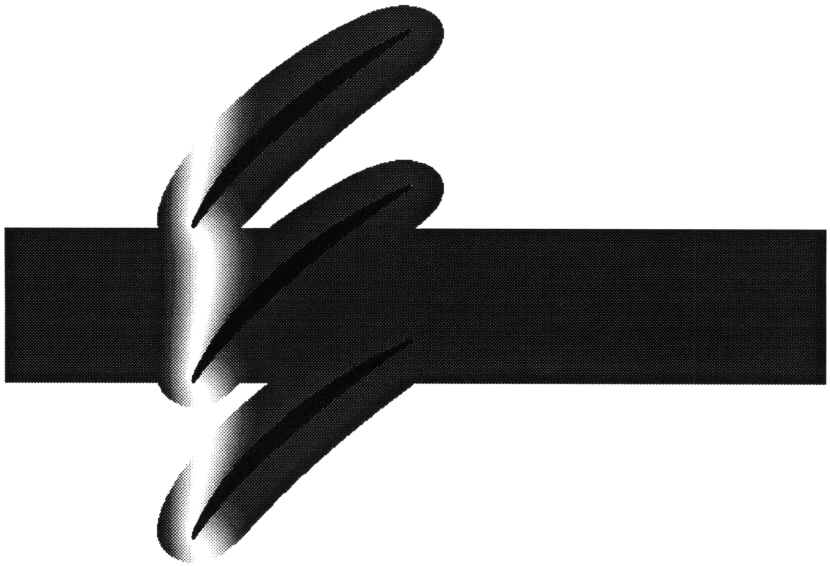

Figure 5.1: Constant density contours for wake near the leading edge with $\rho^* = -\frac{1}{3}$, $\frac{w}{c} = 0.4$ and $\mathrm{Re} = 1e6$.

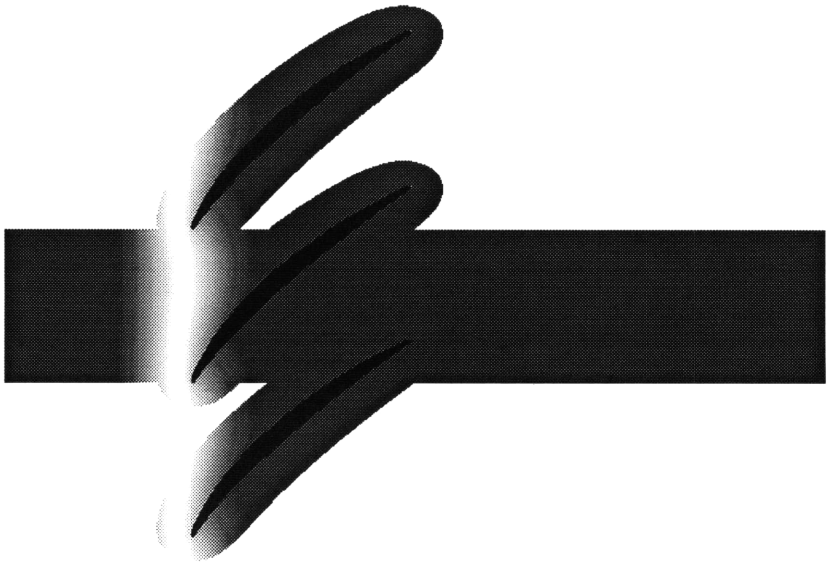

Figure 5.2: Constant density contours for wake near leading edge with $\rho^* = -\frac{1}{3}$, $\frac{w}{c} = 0.5$ and $\mathrm{Re} = 698,671$.

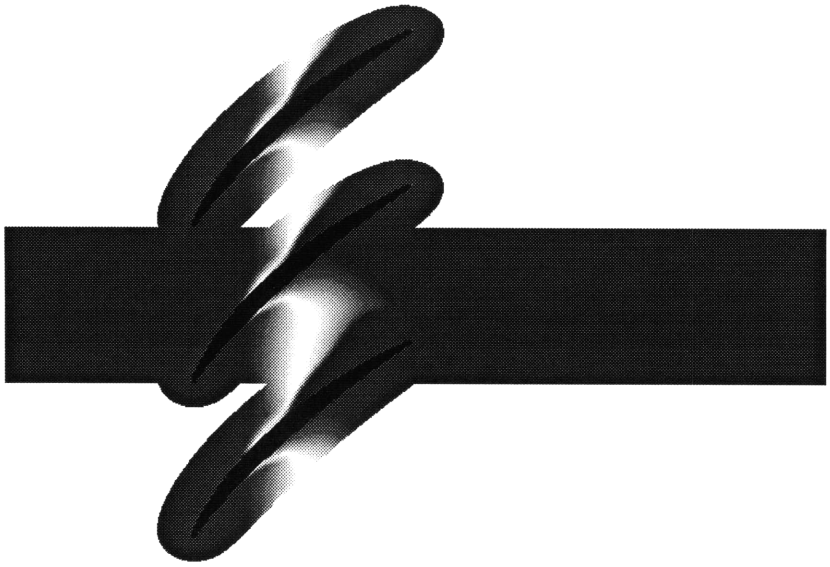

Figure 5.3: Constant density contours for wake near midchord with $\rho^* = -\frac{1}{3}$, $\frac{w}{c} = 0.4$, and $\mathrm{Re} = 1e6$.

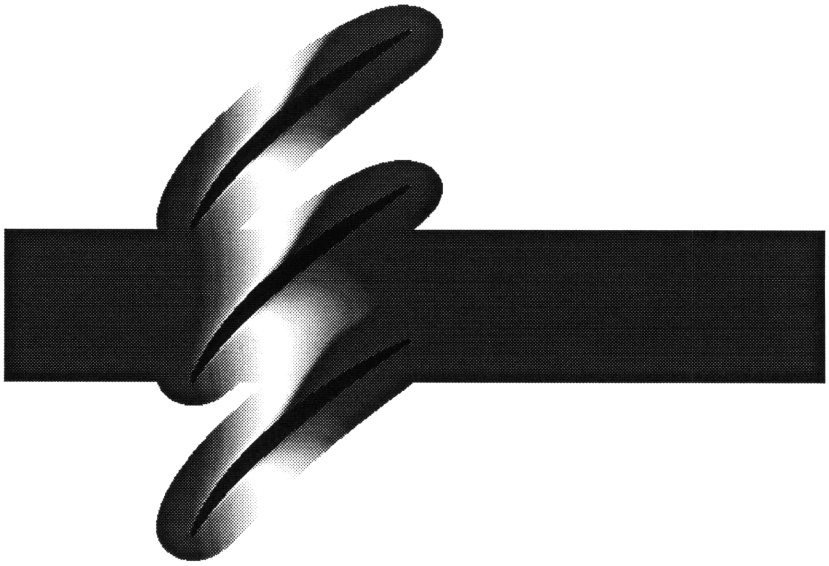

Figure 5.4: Constant density contours for wake near midchord with $\rho^* = -\frac{1}{3}$, $\frac{w}{c} = 0.6$, and $\mathrm{Re} = 698,671$.

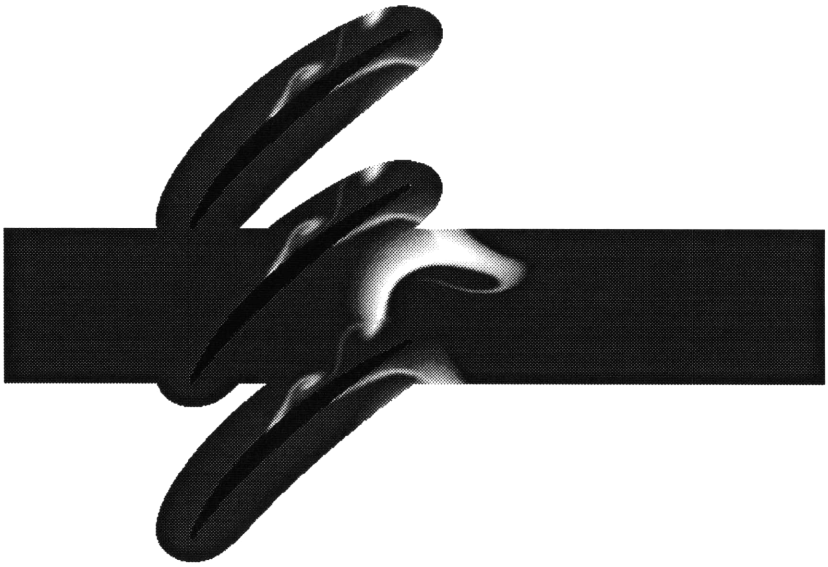

Figure 5.5: Constant density contours for wake near trailing edge with $\rho^* = -\frac{1}{3}$, $\frac{w}{c} = 0.4$, and $\mathrm{Re} = 1e6$.

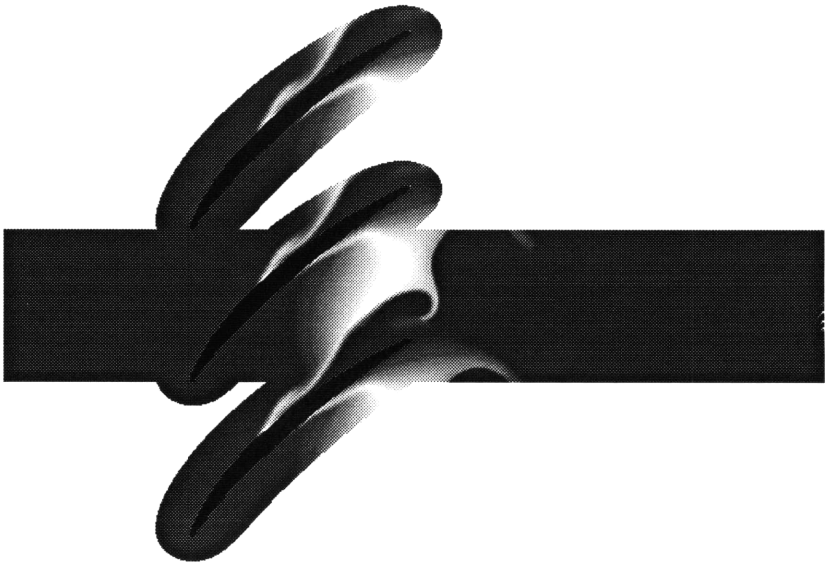

Figure 5.6: Constant density contours for wake near trailing edge with $\rho^* = -\frac{1}{3}$, $\frac{w}{c} = 0.6$, and $\mathrm{Re} = 698,671$.

Figure 5.7: Constant density contours for wake leaving trailing edge with $\rho^* = -\frac{1}{3}$, $\frac{w}{c} = 0.4$, and $\mathrm{Re} = 1e6$.

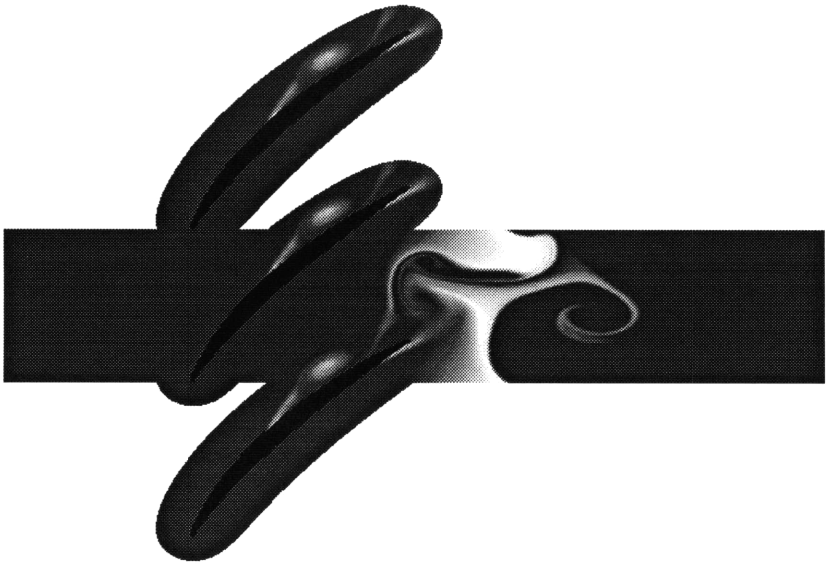

Figure 5.8: Constant density contours for wake leaving trailing edge with $\rho^* = -\frac{1}{3}$, $\frac{w}{c} = 0.6$, and $\mathrm{Re} = 698,671$.

mixed by the shed vorticity much faster than the larger wake of figure 5.8. Smaller density wakes mix with the freestream density faster, and do not appear as a mass of non-uniform density to the next blade row.

5.3 Boundary Layer Interaction

A detailed explanation of the physics involved in the interaction between the boundary layer and the density wake will not be attempted. Because only two test cases were run, not enough information available to gain a clear understanding of the flow field physics. A basic understanding of the interaction can be attained by considering the vorticity equation and boundary layer theory. This yields some insight into the changes in boundary layer characteristics as the density distortion convects through the blade row.

Boundary layer interactions become very complicated because, as seen in figure 5.3, the density distortion convects much slower in the boundary layer then in the rest of the passage. This creates another source of baroclinic torque. At the boundary layer interface with passage flow there is a density gradient in the negative circumferential direction; in front of the boundary layer a gradient exists in the circumferential direction(see figure 5.5 as an example) because part of the wake is greatly slowed in this region near the blade. These density gradients react with the passage pressure rise to create vorticity(see figure 5.9). The region of slowed lower density flow has the greatest effect on the flowfield. The region of low density fluid in front of the separated region causes early separation. The added vorticity (see figure 5.9) reduces the velocity at the blade surface causing early separation. The density gradient formed because the wake flows around the boundary layer also interacts with the axial pressure rise to create vorticity in the passage. This vorticity increases the velocity at the outer edge of the boundary layer and has the effect of reducing the boundary layer because the increased velocity at the edge of the boundary layer provides greater momentum to the fluid. This is verified by the expression

for a turbulent boundary layer thickness:

$$\frac{\delta}{l} \propto Re^{-1/5} \tag{5.1}$$

This effect will be smaller than the effect of the density wake itself. The same

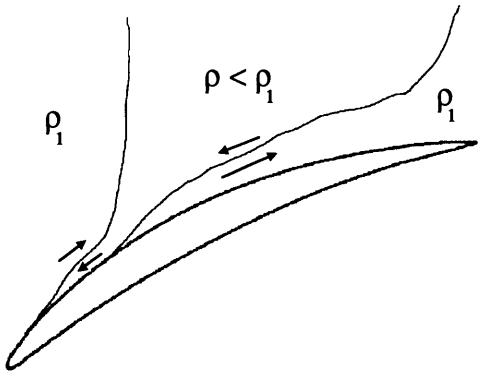

Figure 5.9: Velocity perturbations near boundary layer caused by presence of density gradient.

reasoning explains the effect of the density wake itself. From figure 1.1 two counter-rotating vorticies will be formed when a density wake convects through the passage. For a wake of lower density compared with freestream, the vorticity formed causes a velocity perturbation such as that in figure 4.6. Considering the velocity vectors near the suction side of the blade, the density decrease on the first half of the wake causes an increased velocity near the blade surface. Similarly the increase in density over the back half of the wake causes an axial velocity decrease on the suction side of the blade. Thus the density wake will cause a reduction in boundary layer over the front half of the wake(side nearest the trailing edge) and an increase in boundary layer over the back half of the wake.

The effects of these vorticies on the boundary layer are seen in contour plots of axial velocity from the two tests. Figures 5.10 and 5.11 show the steady state velocity contours. Both test cases were run above design point so the flow is highly separated and unsteady trailing vorticies are shed from the wake. In these contour plots dark shading represents higher speed flow, lighter shades represent slower flow, and the very light and white shades represent negative axial flow. The boundary layer near

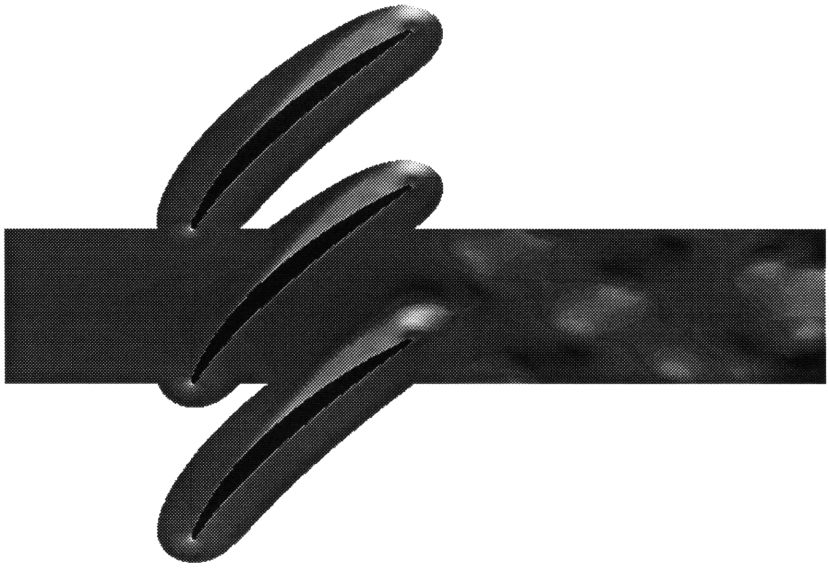

Figure 5.10: Axial velocity contours for steady state flow with Re $= 1e6$.

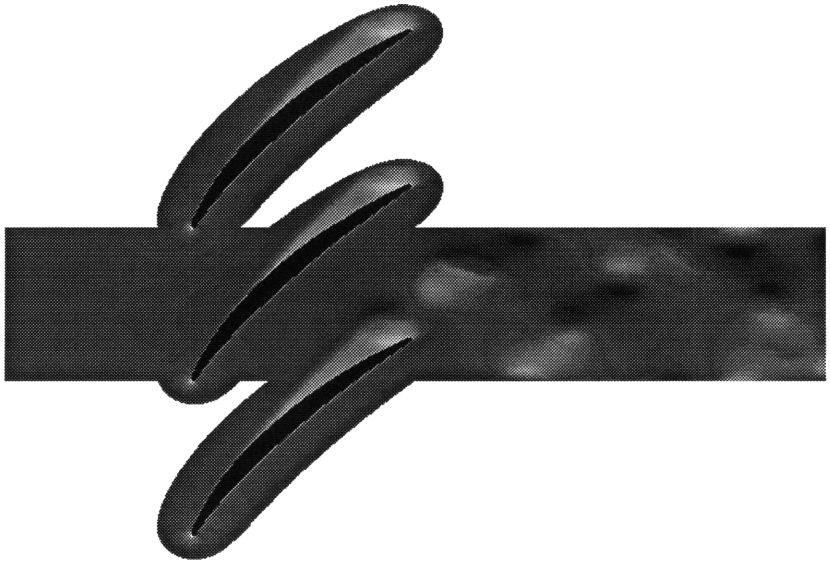

Figure 5.11: Axial velocity contours for steady state flow with Re $= 698,671$.

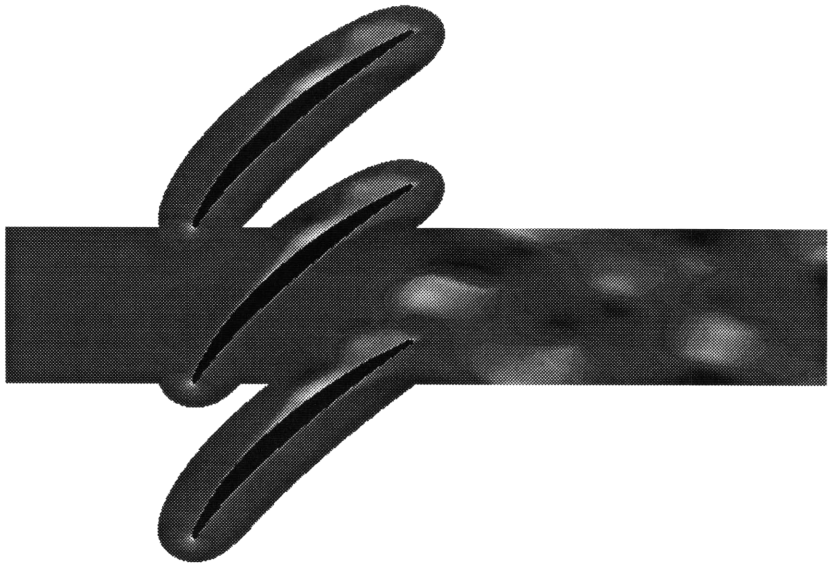

Figure 5.12: Axial velocity contours for wake of figure 5.5

the leading edge is thin for both tests, so interactions will not be clearly visible. Interactions near the trailing edge can not be determined from these tests because the normal growth and decay of the boundary layer due to wake shedding is not available.

The changes which are most noticeable are those which occur because the lower density fluid gets caught in the boundary layer. Figures 5.12 and 5.13 show velocity contours for the test cases corresponding to the wake positions of figures 5.5 and 5.6 respectively. At these positions the wakes are leaving the trailing edge of the blade row. Midchord and just aft of midchord, low density fluid has gotten 'trapped' in the boundary layer because it has a lower momentum. Because of this density variation in the boundary layer region, the boundary layer is larger at the leading edge side of the low density region and is greatly reduced at the trailing edge side of the low density fluid. Figures 5.14 and 5.15 show the velocity contours after this density bubble has traveled to the position of figures 5.7 and 5.8. The bubble is traveling slowly because it is in the boundary layer. The boundary layer at this time has grown but still shows a decrease at the trailing edge side of the density bubble. The density bubble has the effect of reducing the boundary layer downstream of the bubble. As a low

density wake convects through the viscous blade row, a bubble of low density fluid gets caught in the boundary layer. The bubble convects with reduced speed through the passage, and as it does it reduces the boundary layer downstream of the blade row. Just upstream from the center of the bubble the boundary layer is increased from the steady state boundary layer thickness. Upstream of the density bubble the boundary layer thickness is returning to the steady state thickness.

This change in boundary layer behavior has several implications. First the loading changes because the separation region is changing in time. Loading is not the only parameter that is effected. The boundary layer characteristics effect the heat transfer on the blade. From the Reynolds analogy, the heat transfer rate to the blade is proportional to the velocity gradient at the wall:

$$q_w \propto \frac{\partial u}{\partial y} \tag{5.2}$$

As the boundary layer thickness is reduced, the velocity gradient at the wall increases. The local heat transfer rate then increases where local decreases in boundary layer thickness occur. The change in boundary layer thickness also effects performance. The boundary layer displacement thickness

$$\delta^* = \int_{y=0}^{\infty} (1 - \frac{u}{U_\infty}) \mathrm{d}y \tag{5.3}$$

decreases as the boundary layer thickness is reduced, allowing a greater volume flow through the passage. The momentum thickness

$$\theta = \int_{y=0}^{\infty} \frac{u}{U_\infty} (1 - \frac{u}{U_\infty}) \mathrm{d}y \tag{5.4}$$

also decreases, yielding greater momentum flux through the passage. A reduction in the boundary layer as the density wake convects through the passage improves passage performance but causes greater local heat transfer to the blade surface.

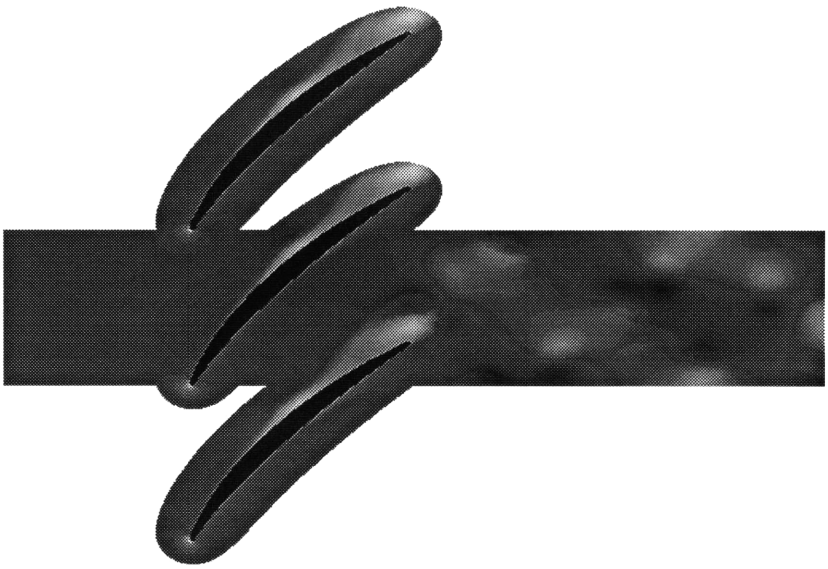

Figure 5.13: Axial velocity contours for wake of figure 5.6

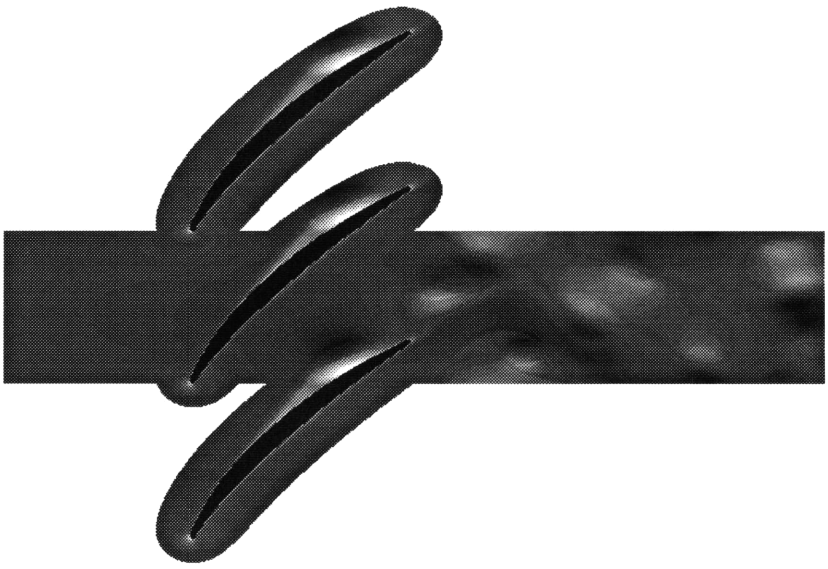

Figure 5.14: Axial velocity contours for wake of figure 5.7

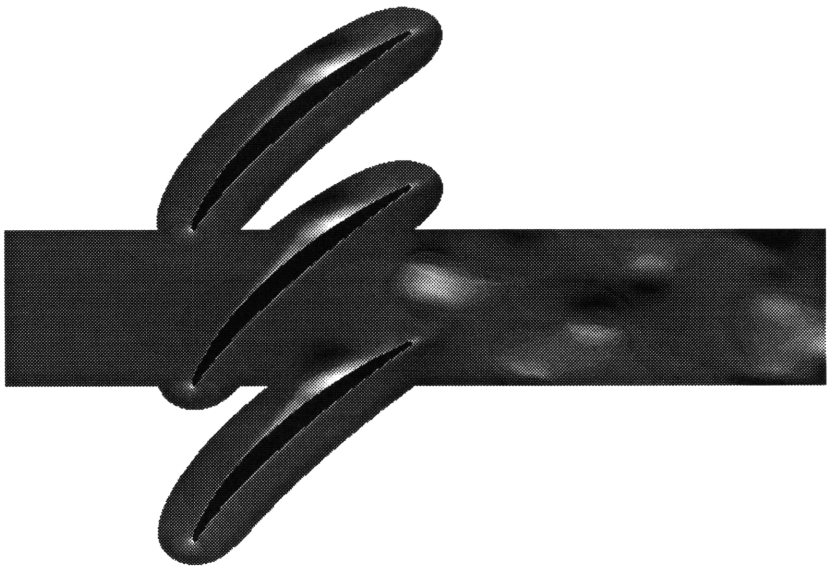

Figure 5.15: Axial velocity contours for wake of figure 5.8

5.4 Summary

As a density wake convects through a viscous fluid, the wake deforms due to slower flow at the blade surfaces. Most of the wake flows around the boundary layer, but a portion closest to the blade surface gets 'caught' in the boundary layer. This low density region causes a local increase in the boundary layer thickness on the leading edge side of the density bubble, moving the separation bubble forward. The low density region becomes caught in a separation vortex. Downstream of this point the boundary layer thickness is greatly decreased. The boundary layer will return to its original thickness distribution as the density bubble leaves the passage. The low density wake thus causes a large reduction in the boundary layer thickness as a low density bubble gets caught in the boundary layer region. The change in boundary layer characteristics change the loading, heat transfer characteristics, and blade row performance. The loading changes because the separation region is changing in time. The boundary layer characteristics also effect the heat transfer on the blade. From the Reynolds analogy, the heat transfer rate to the blade is proportional to the velocity gradient at the wall. So as the thickness is reduced, the heat transfer will increase. A reduction in boundary layer thickness also improves performance because it allows

a greater volume flow and momentum flux through the passage. A reduction in the boundary layer thickness as the density wake convects through the passage changes the blade loading and improves passage performance but causes greater local heat transfer to the blade surface.

Chapter 6

Conclusions and Recommendations

This study began as an exploration into the importance of convecting density wakes on blade rows. The presence of these density distortions causes added vorticity in the flowfield, but the forces caused by this vorticity were unknown. This study has shown that the time varying loads on blades are significant, even for small changes in density. The effects of viscosity and compressibility on these changes in loading is not yet understood.

6.1 Conclusions

To investigate the effects of convecting density distortions on blade rows, a two pronged study was performed. First an inviscid study was performed to elucidate a physical understanding of the problem. The purpose of this inviscid study was to gain an understanding of the flowfield such that the key parameters for changes in lift and moment could be found. The parameters which were found to influence this flow are the blade geometry, blade pressure distribution, density change ρ^*, and density distortion width $\frac{w}{c}$. Two different blade geometries were studied, a highly and symmetrically loaded EEE blade row and a lower front loaded NACA4F blade row. Sinusoidal wake variations were tested on both blade geometries. The changes in lift

for a given wake scale linearly with the steady state lift:

$$\frac{\Delta Cl}{Cl_{steady}} = f(\rho^*, \frac{w}{c}) \tag{6.1}$$

The change in moment also scales with geometry and wake characteristics. For two different blade geometries the change in moment can be scaled with the steady state moment and the blade passage loading:

$$\frac{\Delta Cm}{\psi Cm_{steady}} = f(\rho^*, \frac{w}{c}) \tag{6.2}$$

Although two blades were studied, most numerical experiments used the NACA4F blade row. Two variations of density distribution were studied: a flat top and a sinusoidal density variation. Both types of distortion deform toward one side of the blade passage as they convect through the blade row. Thus they are no longer planar wakes when they enter downstream blade rows. The flat top distortion is simply a variation on the sinusoidal density change. The peak loading asymptotes from the flat top with no constant density section, corresponding to a sinusoidal wake value of $\frac{w}{c} = 0.1$, to $(\frac{\rho_2}{\rho_1})$ times the steady state loading as the front and back density gradients become slightly more than one chord length apart. At this distance the back of the wake is far enough upstream that it does not interact with the pressure potential of the blade row until the front of the wake leaves the trailing edge of the blade.

For typical density gradients found in compressors, a linear relationship between blade loading and $\rho^*(\frac{w}{c})$ was found. For turbines, and possibly even for the EEE blade, this linearity may not hold. The linearity in loading can be attributed not only to the small wake parameter values, but also to the linearity in pressure gradient across the NACA4F blade row. These parameters are vital to the physics of the flowfield and will be important in any more general scalings.

Boundary layer interactions may greatly influence the results found for inviscid flowfields. The two test cases examined for viscous flows indicate that the density change will move very slowly at the blade surface. A density decrease will be caught up by the boundary layer, changing the boundary layer and separation characteristics.

The low density fluid gets caught in the boundary layer and causes the separation bubble to move forward on the blade. Downstream of this point the boundary layer will be much thinner. The bubble of density will then convect down the blade row at a rate slower than freestream, until it leaves the trailing edge of the blade and the flow returns toward the unperturbed state. This change in separation and boundary layer thickness may have a significant effect on time varying loading and heat transfer.

6.2 Recommendations

Preliminary viscous experiments showed a significant interaction between the boundary layer and the density wake. This interaction causes a time varying change in boundary layer thickness and can induce separation on the blade surface. These changes at the boundary layer may alter the blade loading from the inviscid relations found. They may also effect heat transfer on the blade surface and blade row performance. Performing a more quantitative study of boundary layer effects is important for a complete understanding of the significance of this problem. The tests studied in this thesis were performed on compressor blades because they are more susceptible to high cycle fatigue problems. However, turbine blades are more likely to encounter large density distortions. Because the preliminary data indicates varying heat transfer rates on the blade surface, the effects of convecting density wakes on turbine blades may be important to understanding thermal stresses on turbine blades. Several other factors should be included to more closely simulate conditions in real turbomachinery. These factors include compressibility, multiple wakes in a passage, wakes at varying angles to the blade row, and the effects of operating conditions. This thesis shows significant loading changes on blade rows due to convecting density distortions, but several aspects to the problem still need to be investigated.

Bibliography

[1] M. B. Giles. Non-reflecting boundary conditions for the euler equations. CFDL-TR-88-1, Massachusetts Institute of Technology, Computational Fluid Dynamcs Laboratory, February 1988.

[2] Donald Hoying. *Blade Passage Flow Structure Effects on Axial Compressor Rotating Stall Inception.* PdD dissertation, Massachusetts Institute of Technology, Department of Aeronautics and Astronautics, September 1996.

[3] Nelson H. Kemp and W.R. Sears. The unsteady forces due to viscous wakes in turbomachines. *Journal of Aeronautical Sciences*, pages 478–483, July 1955.

[4] J.L. Kerrebrock and A. A. Mikolajczak. Intra-stator transport of rotor wakes and its effect on compressor performance. *ASME Paper 70-GT-39*, 1970.

[5] S.R. Manwaring and D.C. Wisler. Unsteady aerodynamics and gust response in compressors and turbines. *ASME Paper 92-GT-422*, 1992.

[6] F. E. Marble. Response of a thin airfoil encountering a strong density discontinuity. *Journal of Fluids Engineering*, 115:580–589, December 1993. Part of Transactions of ASME.

[7] O. Redlich and F.R. Watson. On programs for tests involving several variables. *Aeronautical Engineering Review*, pages 51–59, June 1953.

[8] C. K. W. Tam and J. C. Webb. Dispersion-relation-preserving finite difference scheme for computational acoustics. *Journal of Computational Physics*, 107:262–281, 1993.

[9] Theodore V. Valkov. Control of unsteady flow in a stator blade row interacting with upstream moving wakes. Master's thesis, Massachusetts Institute of Technology, Department of Aeronautics and Astronautics, May 1992. Also GTL report no. 255.